Icarus 382 (2022) 114939

Contents lists available at ScienceDirect

Icarus

journal homepage: www.elsevier.com/locate/icarus

The global thermophysical properties of (433) Eros

M.L. Hinkle[a,*], E.S. Howell[b], Y.R. Fernández[a], C. Magri[c], R.J. Vervack Jr[d], S.E. Marshall[a,e], J.L. Crowell[f], A.S. Rivkin[d]

[a] University of Central Florida, Orlando, FL, USA
[b] Lunar and Planetary Laboratory, University of Arizona, Tucson, AZ, USA
[c] University of Maine at Farmington, Farmington, ME, USA
[d] Johns Hopkins University Applied Physics Laboratory, Laurel, MD, USA
[e] Arecibo Observatory, Arecibo, PR, USA
[f] Naval Information Warfare Systems Command, United States Navy, San Diego, CA, USA

ARTICLE INFO

Keywords:
Near earth
Asteroid
Thermophysical
Near infrared
Eros

ABSTRACT

We present results from a shape-based, rotationally-resolved thermophysical model of near-Earth asteroid (433) Eros, using reflected and near-IR spectra collected at the NASA Infrared Telescope Facility (IRTF) over 18 nights (25 disk-integrated spectra in total) from 2009 to 2019. The data sample a variety of viewing geometries, illumination angles, and rotational phases and therefore allow us to characterize Eros's surface physical properties in detail, particularly at wavelengths in the thermal near-IR regime ($\lambda > 3.5$ μm) that were not measured by the NEAR Shoemaker mission. Eros's shape, spin state, density, albedo, and other physical properties measured by NEAR were incorporated into our model, leaving thermal inertia and surface roughness as free parameters. We find that a thermal inertia range of 100–150 J m^{-2} K^{-1} $s^{-1/2}$ and a roughness crater fraction of 0.3–0.4 with crater opening angle 130° (equivalent adirectional rms slope angle of 32° +/− 4°) fit data from 18 spectra at the 1σ level, but do not fit the remaining 7 spectra. This suggests that Eros's thermal properties vary over its surface, which has important implications for linking remote sensing data to spacecraft measurements of the physical properties of near-Earth asteroids.

1. Introduction

Accurately constraining the physical properties of near-Earth asteroids (NEAs) is crucial to understanding the origins of the solar system, planning for spacecraft missions, determining the provenance of meteorites, and assessing the impact hazard. Thermophysical models (TPMs) are powerful tools for characterizing airless bodies in the solar system using remote sensing data as constraints. However, the accuracy of a TPM depends critically on knowledge of an asteroid's physical parameters such as shape, size, rotation state, and albedo. Understanding those properties as accurately as possible reduces the number of free parameters in the model and thus enables focused investigation of the effects of other properties, such as thermal inertia and surface roughness. Spacecraft measurements of NEA physical properties are the gold standard when it comes to knowledge of the physical parameters; therefore, using these "ground truth" data in TPMs can improve our understanding of the quantitative effects of thermal inertia and surface roughness on disk-integrated asteroid spectra generally acquired from the ground.

One of the best studied NEAs is (433) Eros, which was explored by the NEAR Shoemaker spacecraft in 2000–2001 (hereafter referred to as NEAR). The NEAR near-infrared spectrometer (NIS) observed Eros's near-IR reflectance (0.8–2.6 μm), but not its thermal emission (Veverka et al., 1997; Warren et al., 1997). Thermal observations of Eros were first reported by Morrison (1976) and Lebofsky and Rieke (1979). Their ground-based photometric observations were made at 1.25–22.0 μm. They analyzed these observations using an elongated shape model, rotation period of 5.27 h, and pole orientation of RA = 15 ± 2° and DEC = 15 ± 5°, all obtained from photometry of Eros. They obtained a thermal inertia of 225 ± 75 J m^{-2} K^{-1} $s^{-1/2}$. Harris and Davies (1999) made photometric measurements of Eros at 25 wavelengths between 8.06 and 13.04 μm. They used a NEATM model (Harris, 1998), assumed a spherical shape, and found thermal inertia ~170 J m^{-2} K^{-1} $s^{-1/2}$. Their data were re-analyzed by Mueller (2007), who used Eros's shape model, pole orientation, and rotation rate from NEAR in a thermophysical model to obtain thermal inertia 100–200 J m^{-2} K^{-1} $s^{-1/2}$ and a crater fraction (a well known proxy for surface roughness) of 0.6 with opening

---

[*] Corresponding author.
E-mail address: mary.hinkle@knights.ucf.edu (M.L. Hinkle).

https://doi.org/10.1016/j.icarus.2022.114939
Received 2 December 2021; Received in revised form 4 February 2022; Accepted 8 February 2022

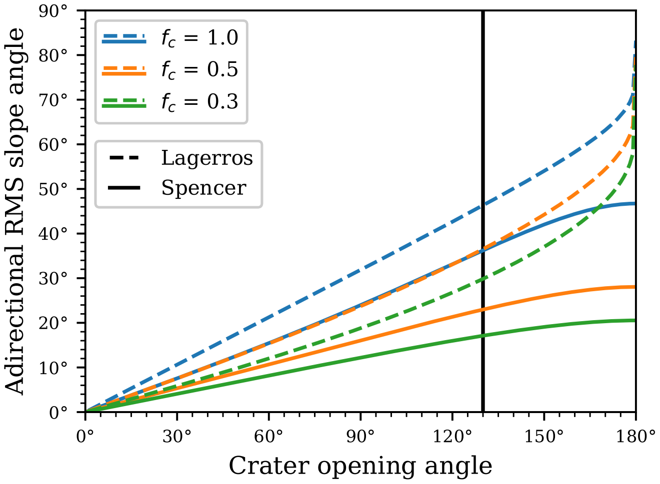

Fig. 1. The vast majority of TPMs model surface roughness by populating some fraction of each shape model facet with spherical-section craters, following the method of either Lagerros (1998) or Spencer (1990). Converting surface roughness crater fraction f_c and crater opening angle to the equivalent adirectional rms slope angle allows direct comparison between Lagerros-like roughness and Spencer-like roughness. The vertical line shows the opening angle $\gamma = 130^\circ$ used in this work.

angle 144° (equivalent rms slope 44.4°, see Fig. 1). Rozitis (2017) reanalyzed the 8–13 µm spectra of Lim et al. (2005) using their shape-based TPM, obtaining a surface roughness adirectional rms slope angle 38° +/− 5°. These previous works utilized observations of Eros at mid-infrared wavelengths, near the peak of its Planck function curve at 9.5 µm, though the two earliest studies also included some NIR photometry. Rivkin et al. (2018) observed Eros's NIR spectrum using the NASA IRTF SpeX instrument over 7 nights in 2011–2012. They used a modified STM (Lebofsky et al., 1986) to estimate Eros's global average thermal inertia at 167 ± 98 J m^{-2} K^{-1} s$^{-1/2}$.

We investigate the global thermal properties of Eros using near-IR wavelength data obtained from numerous vantage points to constrain our TPM. Observations of Eros made at a variety of heliocentric distances, rotational phases, and viewing and illumination geometries reveal whether a single set of thermal parameters can accurately describe many different rotationally-resolved observations. Section 2 describes our observations of Eros using the NASA IRTF on 18 nights over 2009–2019, Section 3 presents TPM results for rotationally-resolved NIR spectra of Eros, and Section 4 discusses the analysis of Eros's surface properties as derived from our TPM results.

2. Spectral observations of (433) Eros

We observed Eros at the NASA IRTF on 12 nights (18 disk-integrated spectra) spanning 2009–2019, using the SpeX instrument (Rayner et al., 2003) in both prism and long wavelength cross-dispersed (LXD) modes. Prism mode covers 0.8–2.5 µm with resolution $R = 200$ pre-2014 and 0.7–2.5 µm with R = 200 post-2014. LXD mode covers 1.95–4.2 µm with $R = 2000$ pre-2014 and 1.98–5.2 µm with $R = 2500$ post-2014. The observational circumstances of our observations are shown in Table 1.

Observations were taken in pairs by "nodding" the telescope by 10 arcseconds along the 15 arcsecond slit between exposures in a standard ABBA pattern, which allowed for sky subtraction. We used the 0.8 arcsecond wide slit and rotated the instrument to align the slit with the parallactic angle to minimize differential refraction. We did not use the dichroic filter, but instead guided using the light reflected from the slit

Table 1
Observational circumstances for our IRTF SpeX observations of (433) Eros used in thermophysical modeling. The UTC date and mid-time of observation are also listed. LXD observations in February and March 2019 were divided into 3 separate sums in order to investigate rotational variability of Eros's thermal parameters; the mid-time of each sum is listed. The asteroid's heliocentric distance (r) and geocentric distance (Δ) are given in au, and the solar phase angle α in degrees. The nearby calibration and solar analog stars used to reduce the data are listed in the final column.

Date (UTC)	Mid-time (UTC)	Integration time (seconds)	SpeX mode	r (au)	Δ (au)	α	Nearby calibration and solar analog stars
05 Nov 2009	05:01:59 04:53:58	160	Prism LXD	1.527	0.927	38.7	SAO 90339, SAO 73225, SAO 111270, SAO 93936
06 Nov 2009	04:53:35 04:59:43	120	Prism LXD	1.524	0.933	39.0	SAO 90339, SAO 73225, SAO 111270, SAO 93936
06 Dec 2011	14:20:55 14:27:24	48	Prism LXD	1.177	0.329	47.6	SAO 93936, SAO 131516, SAO 60387, SAO 72694, SAO 111157, SAO 54620, SAO 129922
02 Aug 2018	14:04:21 14:36:14	465	Prism LXD	1.590	1.181	39.6	SAO 94049, SAO 13670, SAO 74767
08 Sep 2018	11:30:53	399	LXD	1.483	0.818	40.2	SAO 74146, SAO 21850
17 Sep 2018	10:36:44 11:02:26	400	Prism LXD	1.455	0.740	39.8	SAO 31899, SAO 74146, SAO 141976, SAO 39061, SAO 74636
20 Nov 2018	14:32:23 14:18:29	81	Prism LXD	1.253	0.333	32.5	SAO 98710, SAO 15497
28 Nov 2018	13:43:54 14:01:13	134	Prism LXD	1.230	0.302	31.8	SAO 98710, HD 103592
18 Jan 2019	09:24:40 09:41:02	200	Prism LXD	1.138	0.209	38.6	SAO 98710, SAO 153080, SAO 153099, HD 33169
12 Feb 2019	06:06:17 05:44:44 06:44:51 07:17:30	211 311 311	Prism LXD (A) LXD (B) LXD (C)	1.136	0.244	47.3	SAO 94049, SAO 94658
15 Mar 2019	08:10:45 05:44:44 06:44:51 07:17:30	161 156 156	Prism LXD (A) LXD (B) LXD (C)	1.175	0.351	51.3	SAO 98710, SAO 114915, SAO 112615
21 Mar 2019	08:23:20 08:37:19 08:53:58 09:11:40	156 156 156	Prism LXD (A) LXD (B) LXD (C)	1.188	0.377	51.2	SAO 78236, SAO 98710, SAO 115559, SAO 115983

jaws in the 1.5–2.5 μm region (H and K) filters. In addition to Eros, we observed a nearby calibration star within about 10° of Eros and an additional well-characterized solar analog star on each night. The solar analog star was used to correct the slope of the nearby calibration star to that of the Sun via a low-order polynomial fit, if necessary. Details about the selection and use of solar analog stars are given in Lewin et al. (2020). The colors of all nearby stars were chosen to be as close to solar colors in visible and near-infrared (JHK) as possible, and the spectra were checked for non-solar features and unexpected slopes.

SpeX data were reduced using the SpeXtool software package (Cushing et al., 2004) Although Eros is often bright enough to reduce individual pairs of spectra, we summed the observation pairs before extracting the spectra. For each pair within the given sum, the background signal was fitted to each column and removed. A median spatial profile was created for each order. The region inside the aperture and the background on each side was selected by hand to match the seeing in the resulting spectrum. A constant or linear fit to the background in the spatial dimension was carried out and removed. The spectral orders were adjusted where they overlapped and then combined. The entire spectrum was resampled at 0.001 μm over the LXD range. The effective spectral resolution is much higher than we need for thermal modeling, so we binned the LXD spectrum by 25 pixels to improve the signal-to-noise ratio (SNR).

To correct for water vapor in prism spectra, we used Bus's method (described by Rivkin et al., 2004) with some minor modifications. Telluric correction for LXD spectra was done via the method of Volquardsen et al. (2007). Our observations of Eros are part of a larger observing campaign to characterize the properties of near-Earth asteroids in the near-IR, and further details on calibration, extraction of spectra, and data processing of pre-upgrade SpeX data are described by Howell et al. (2018).

Our data are supplemented by 6 nights (7 disk-integrated spectra) of published IRTF SpeX LXD spectra of Eros from 2011 (August and October) and 2012 (January, May, June, and July) from Rivkin et al. (2018). This brings the total number of disk-integrated spectra to 25 (see Table 1). We also obtained optical spectra of Eros from the MINUS campaign (Binzel et al., 2004) and the Eight Color Asteroid Survey (Zellner et al., 1985). The optical spectra were combined with our prism spectra and used (as the asteroid's reflectance behavior) as an input to the thermal model. These and other thermal model parameters are discussed in Section 3.

3. Thermophysical model of (433) Eros

3.1. Thermophysical model description

We modeled Eros's thermal spectrum at each observational epoch using the thermophysical modeling code SHERMAN, which is briefly described here. Further details are discussed by Magri et al. (2018) and Howell et al. (2018). SHERMAN incorporates Eros's shape model and rotation state, as well as the asteroid's position with respect to Earth and the Sun, in order to solve the 1-D heat equation over the asteroid surface. The resulting thermal flux distribution is then integrated over the surface area of the asteroid that is visible to the observer to generate a synthetic spectrum.

Eros's shape is represented as a mesh of 2200 triangular facets, coarsened from the original 65,000 facets of Gaskell's shape model (Gaskell, 2008) as the lower resolution is sufficient for our purposes and greatly speeds up computation time. Topographic features on Eros, such as impact craters and ridges, can shadow nearby facets, reducing their insolation and thus lowering their thermal emission. Conversely, the walls of large impact features such as Himeros Crater and Psyche Crater experience mutual heating effects that enhance their thermal emission. Both of these effects depend on the insolation direction, orientation of Eros's spin vector, and the asteroid's rotation phase. We utilized the spin state of Veverka et al. (2000), derived from NEAR observations, for the models presented here.

Table 2
Thermophysical parameters used in our model of (433) Eros. Rotation period, p_v, and bulk density are all spacecraft measurements. H, G, and p_v are used to calculate Hapke scattering coefficients (Verbiscer and Veverka, 1995). Emissivity of 0.9 was assumed. The opening angle of surface roughness craters was chosen to be consistent with other NEAs thermal models utilizing SHERMAN (Marshall et al., 2017; Howell et al., 2018; Jones, 2018).

Parameter	Value	Reference
H	11.16	Tholen (2009)
G	0.46	Tholen (2009)
Rotation period	5.27026 ± 0.000002 h	Yeomans et al. (2000)
Geometric albedo (p_V)	0.25 ± 0.06	Veverka et al. (2000), Binzel et al. (2004)
Bulk density	2.67 ± 0.03 g/cm^3	Yeomans et al. (2000)
Roughness crater opening angle (γ)	130°	Assumed
Emissivity (ε)	0.9	Assumed

Sub-facet scale roughness is modeled via spherical section craters that uniformly populate a user-specified fraction of each shape model facet, following the method described in Lagerros (1998) and Magri et al. (2018), in which heat conduction within the craters is ignored. For now, we consider the roughness crater fraction to be homogeneous over the entire asteroid surface, though SHERMAN can handle variations across the surface. A full crater opening angle (γ) of 130° was chosen to be consistent with other SHERMAN models of S-type asteroids (Marshall et al., 2017; Howell et al., 2018; Jones, 2018). It is important to note that Spencer's (1990) roughness model defines opening angle γ as the polar angle θ of the spherical section crater, but the Lagerros-style roughness craters in our thermophysical model use the full opening angle 2θ. Mutual heating of elements within these craters influences the bulk thermal emission (and reflected light) from the asteroid: a rough surface has many elements that can "see" one another, so will be hotter than a smooth surface.

We use the Lagerros (1998) treatment of surface roughness, and it is useful to see how this differs from modeling by others who use the Spencer (1990) treatment. Spencer (1990) and Lagerros (1998) use different methods for quantifying the roughness of a surface when a fraction f_c of that surface is covered by identical spherical-section craters with full opening angle γ. (Lagerros actually gives his expression in terms of $S = \sin^2(\gamma/4)$, the ratio of the crater's depth to the diameter of its defining sphere.) There are two substantive differences between the two methods. First, Lagerros computes dimensionless rms slope ρ, while Spencer computes s, the rms slope angle in degrees. Since the slope is the tangent of the slope angle, s remains finite as γ approaches 180° but ρ goes to infinity. Second, Lagerros gives the one-dimensional rms slope, computed from slopes measured along a 1-D transect across the surface, while Spencer gives the adirectional rms slope angle, computed using the steepest slope angle at each point on the surface. For an isotropic surface, the adirectional rms slope is just $\sqrt{2}$ times the 1-D version. Thus one can sensibly compare $s' = \tan^{-1}(\rho\sqrt{2})$ with s: for any given value of f_c, these two quantities are similar at small γ (smooth surfaces) but diverge at large γ (rough surfaces) as ρ approaches infinity (see Fig. 1). It should be stressed that both ρ and s are plausible measures of roughness, with neither being intrinsically superior to the other.

In addition to shape and surface roughness, SHERMAN requires many user-specified constraints on the asteroid's physical properties such as optical scattering law, surface roughness, thermal inertia, IR emissivity, density, geometric albedo, and spin state. In our model of Eros, we fix many of these parameters to direct measurements by the NEAR spacecraft: Eros's spin state, geometric albedo p_v, and bulk density, as well as the shape model (Gaskell, 2008), are all constrained by spacecraft data. Optical scattering law (Hapke) coefficients were obtained from Eros's H magnitude, G parameter, and geometric albedo using the method of Verbiscer and Veverka (1995). Emissivity is

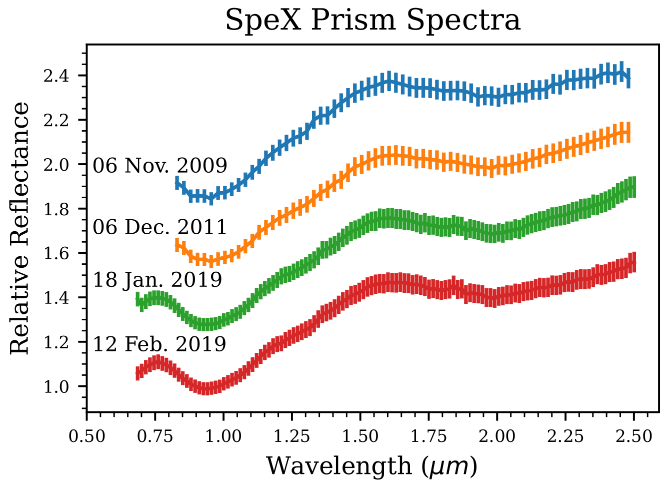

Fig. 2. Several sample SpeX prism spectra, normalized at 0.9 μm and offset for clarity. Prism spectra obtained prior to the 2014 SpeX upgrade covered 0.84–2.5 μm, post-2014 spectra cover 0.7–2.5 μm. Eleven prism spectra in total were collected (see Table 1). These were averaged together along with archival data from SMASS and ECAS to produce the average reflectance spectrum that we used in our thermophysical modeling (see Fig. 3). The remaining prism spectra are shown in Appendix A.

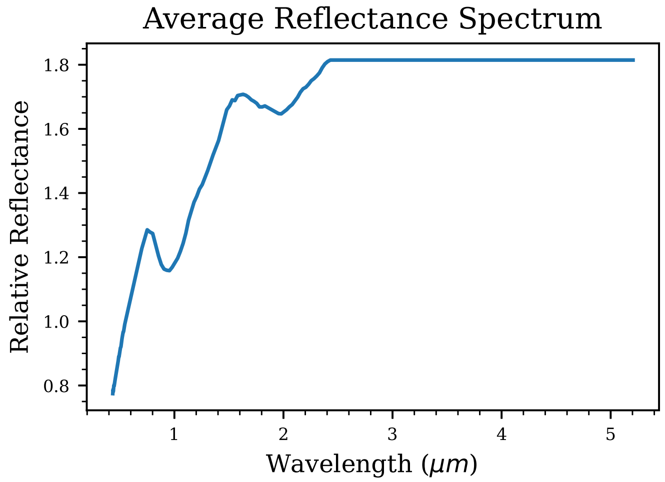

Fig. 3. The average reflectance spectrum used to model Eros using SHERMAN. This is the average of our SpeX prism data from 0.70–2.5 μm; the reflectance spectrum is assumed to be flat at wavelengths longer than 2.3 μm. From 0.44–0.70 μm, we average an Eros SpeX prism spectrum from SMASS (Binzel et al., 2004) with Eros spectrophotometry from the ECAS (Zellner et al., 1985) and prepend the averaged spectrum to our own averaged prism data to create an average reflectance spectrum that covers 0.44–2.5 μm, normalized to 1.0 at 0.55 μm.

assumed to be 0.9, which is consistent with laboratory measurements of silicate materials (Ostrowski and Bryson, 2020; Maturilli et al., 2016), and discussed further in Sections 3.2.2 and 4.1. Values for fixed parameters incorporated in our thermal model of Eros, including the assumed roughness crater opening angle, are listed in Table 2. Thermal inertia (hereafter TI) and surface roughness (crater fraction, hereafter CF) were the only parameters varied within the thermal models of Eros presented here.

In addition to geometric albedo, SHERMAN also incorporates Eros's reflectance spectrum as a model input parameter. We averaged our SpeX prism data (sample spectra shown in Fig. 2) for Eros and appended shorter wavelength data from the Small Main Belt Asteroid Spectroscopic Survey (SMASS) and Eight Color Asteroid Survey (ECAS) to obtain an average reflectance spectrum for Eros (Fig. 3) and used this as a SHERMAN input parameter.

SHERMAN is initialized 10 Eros rotation periods before the time of observation in order to allow enough time for the diurnal wave to penetrate the assumed 10 thermal skin depths and 20 depth layers per thermal skin, which stabilizes the surface and sub-surface temperatures by permitting the model to "forget" the initial conditions. The choice of 10 rotations is arbitrary but has been shown to be sufficient to stabilize the surface temperature in our TPMs, which is discussed in detail in Magri et al. (2018). In general, when initializing the surface temperatures of a shape model we check to see whether for any facet the temperature has not stabilized after 10 rotations. If so, the initial conditions are adjusted and integrated over ten rotations again. Lateral heat conduction is ignored.

We modeled Eros's thermal emission spectrum for the 25 disk-integrated spectra corresponding to our own observations made at the IRTF and those of Rivkin et al. (2018). We calculated each model using its respective observation geometry in order to determine which sets of thermal inertia and surface roughness parameters best characterize each observation. Each model's fit to the respective observed spectrum was evaluated via a weighted χ^2 test. The data were weighted by wavelength so that $\lambda > 4.5$ μm (for post-2014 data) and $\lambda > 3.5$ μm (pre-2014 data) were three times as important as the shorter wavelengths. Fitting the reflectance-dominated region of the model to the data is less important than fitting the thermal region because Eros's reflectance spectrum is one of SHERMAN's model inputs, so the computed spectrum matches the input reflectance shortward of 2.3 μm where the thermal is negligible by construction. Each model's χ^2 is then normalized by setting the lowest χ^2 value of the ensemble of model fits to 1.0; this normalized χ^2 then describes the relative goodness-of-fit within each observation's ensemble of models. The best-fitting thermal parameters for each individual spectrum are shown in Fig. 4.

Note that the 1σ uncertainty for each of the IRTF SpeX LXD spectra is calculated for the relative reflectance at each wavelength. This is a combination of photon error in the original raw asteroid and stellar calibrator data, and systematic error from uncertainty in the atmospheric corrections and observing conditions. Several spectra are averaged together from each asteroid measurement and standard star pair, and then points are binned in wavelength for the final spectrum. The variance for each point is compared with the random error combined in quadrature, and the larger of the two measurements is assigned to that point. Even at the final resolution, the spectrum is oversampled, and the spectral points are not independent. By normalizing each χ^2 we account for any changing systematic differences due to the data points not being independent.

3.2. *Thermophysical model results*

3.2.1. *Near-infrared*

Our goal was to find a common set of thermal parameters (thermal inertia and crater fraction) that would fit all 25 individual disk-integrated spectra, and therefore would constrain the average thermal properties of Eros's surface. However, we found that no single pair of values for the two thermal parameters would fit all of the Eros observations simultaneously. Maps of the chi-square test results for the ranges of thermal parameters tested are shown in Fig. 4, and the data and model LXD spectra for 4 example cases are shown in Fig. 5.

Fig. 4 shows maps of χ^2 for our model fitting; each panel in that figure corresponds to one of our 25 spectra. The χ^2 has been normalized in each panel as described in Section 3.1. Values of normalized χ^2 were then estimated to be equivalent σ confidence intervals for comparing between spectra. Within each panel of Fig. 4, each colored square indicates a model generated with the corresponding values of thermal inertia and crater fraction, with colour indicating the confidence level at which that model fits the data. All models that fit within the 1σ uncertainty are indicated by yellow squares. Similarly, models that fit within

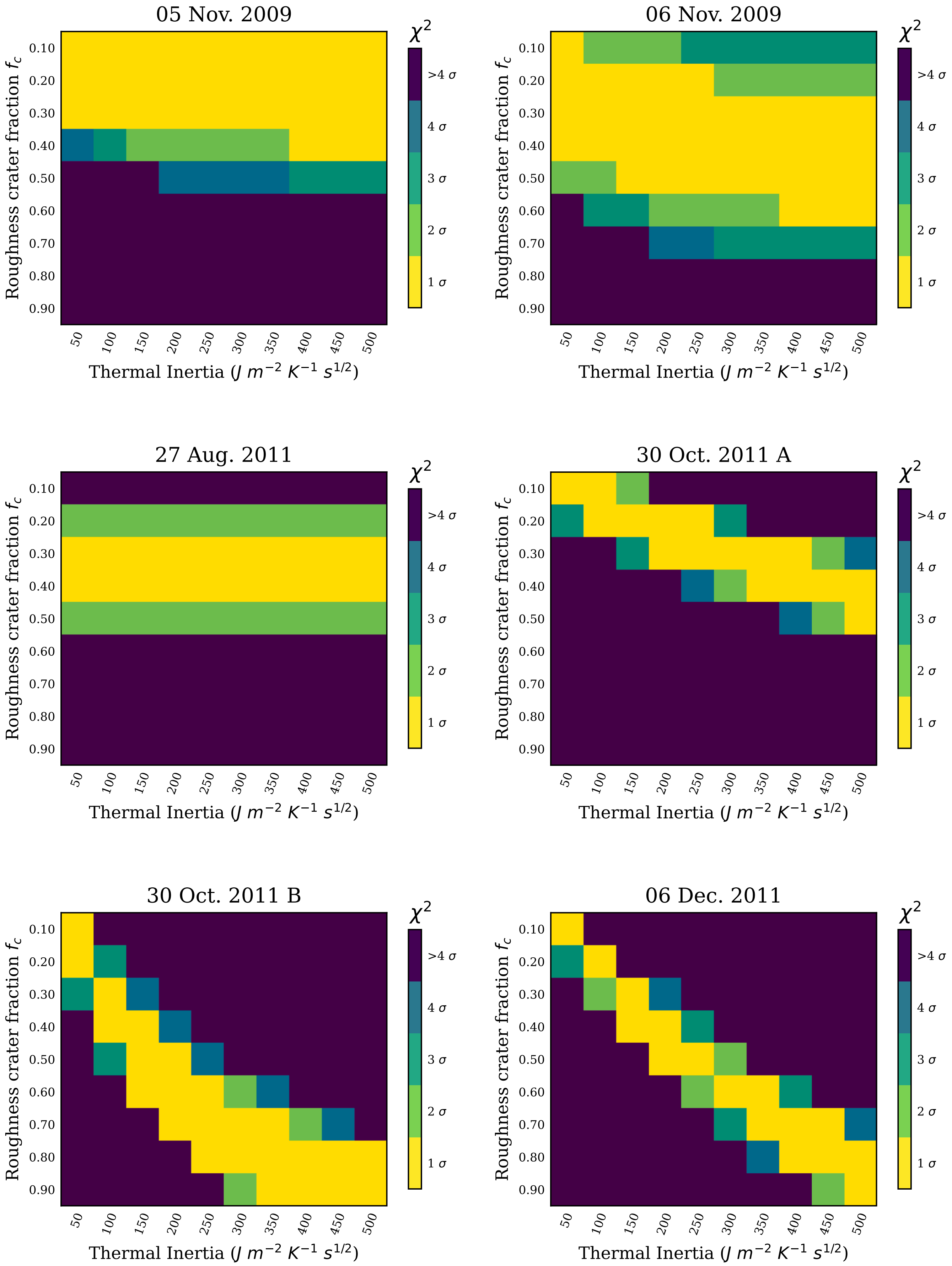
05 Nov. 2009
06 Nov. 2009
27 Aug. 2011
30 Oct. 2011 A
30 Oct. 2011 B
06 Dec. 2011
Roughness crater fraction f_c
0.10
0.20
0.30
0.40
0.50
0.60
0.70
0.80
0.90
Thermal Inertia ($J\ m^{-2}\ K^{-1}\ s^{1/2}$)
50
100
150
200
250
300
350
400
450
500
χ^2
>4 σ
4 σ
3 σ
2 σ
1 σ

Fig. 4. Model results in thermal inertia-crater fraction (roughness) space for all 25 disk-integrated spectra. Each panel is a colour-coded 10 × 9 plot of "relative" χ^2 in terms of uncertainty (see text), corresponding to the 90 sets of parameters we tried for each observation. Each colored square within a panel corresponds to a single model. Models that fit at the 1-sigma level are indicated in yellow, 2-sigma in green, 3-sigma in light blue, and so on; see Section 3.2 for details on how these confidence intervals were calculated. For 9 of our 25 observations, the modeling resulted in no constraint on thermal inertia; these appear as panels with fairly horizontal colour contours. In the remaining 16 cases, the degeneracy between thermal inertia and surface roughness estimates in diagonal or banana-shaped contours. (For interpretation of the references to colour in this figure legend, the reader is referred to the web version of this article.)

the 2σ uncertainty are indicated by green squares, within the 3σ uncertainty by blue squares, within 4σ uncertainty by indigo squares, and models that fall outside >4σ by purple squares. While not completely rigorous, the fits of spectra within a group are consistent and the model curves that fall 2σ are generally twice the assigned errorbars from the data in the 3.5–4.5 μm regions. We believe this is a conservative approach to combining the goodness-of-fit for multiple spectra within each group.

Ninety sets of model parameters were tested for each spectrum, forming the 10 × 9 grid of colored squares in each panel. Thermal inertia was tested in increments of 50 J m^{-2} K^{-1} $s^{-1/2}$ and crater fraction in increments of 0.1. We also tested the same parameter space at a finer resolution of 25 J m^{-2} K^{-1} $s^{-½}$ and 0.05 (Fig. C1) and found that the results agreed with the coarser resolution grid. Therefore, we assume that interpolation between squares on the contour plots in Figs. 5 & 10 is acceptable. The synthetic spectra change smoothly, as expected, with changes in input parameters. Note that there are clearly two general shapes of contours in the panels: those with mainly horizontal contours, and those with diagonal (or banana-shaped) contours. Panels with horizontal contours indicate little sensitivity to thermal inertia. Those with diagonal contours indicate correlation between our estimates of the two parameters. Thermal inertia decreases the surface temperature by spreading the heat over more of the surface, while surface roughness increases surface temperatures from effects of self-heating. Thus we find equivalent models can result from different combinations of thermal parameters. Owing to the degeneracy between thermal inertia and crater fraction, even well-constrained contours (e.g. 12 February 2019 A) have at least two best-fitting (yellow squares) sets of thermal parameters.

Each spectrum is generally fit best by one of three locales in parameter space (discussed at greater length in Section 4). Models with TI = 100–150 J m^{-2} K^{-1} $s^{-1/2}$ and CF = 0.3–0.4 (henceforth locale A) fit most of our data – 18 of the 25 spectra – to within 1σ. Models with TI = 300–400 J m^{-2} K^{-1} $s^{-1/2}$ and CF = 0.3–0.4 (henceforth locale B) fit 6 of the remaining spectra – all the spectra in March 2019. The last remaining spectrum, from January 2019, is best fit by a quite different set of parameters, TI = 300 J m^{-2} K^{-1} $s^{-1/2}$ and CF = 0.9 (henceforth locale C).

In Fig. 5, we demonstrate the differences in fit quality for each spectrum among these three locales in the TI-CF thermal parameter space. In each panel, the orange solid line shows the model for a representative set of locale A parameters (TI = 100–150 J m^{-2} K^{-1} $s^{-1/2}$; CF = 0.3–0.4), the green dashed line shows the model for a representative set of locale B parameters (TI = 300–400 J m^{-2} K^{-1} $s^{-1/2}$; CF = 0.3–0.4), and the red dash-dot line shows the model for a representative set of locale C parameters (TI = 300 J m^{-2} K^{-1} $s^{-1/2}$; CF = 0.9). No single set of average thermal parameters that fits every observation adequately.

3.2.2. *Mid-infrared*

We also used SHERMAN to model 3 mid-IR (8.0–13.1 μm) spectra obtained from the SpectroCam-10 instrument on the 200" Hale telescope at Palomar Observatory (Lim et al., 2005). These same 3 spectra were analyzed by Rozitis (2017) who found that due to the illumination and viewing geometry of the observations, thermal inertia has a negligible effect on the thermal model spectrum. This more or less "pole-on" observing geometry cannot constrain thermal inertia (see Section 3.2 & Fig. 6), so our mid-IR models employed a fixed thermal inertia of 150 J m^{-2} K^{-1} $s^{-1/2}$ and only fit surface roughness. We scaled our mid-IR models by an arbitrary scaling factor similar to that used by Rozitis (2017).

We found that when using the same geometric albedo $p_v = 0.25$ as in our NIR models, the mid-IR spectra required an average roughness crater fraction of 0.5–0.9 (Fig. 7), which is higher than our NIR average of 0.3–0.4 (see Section 3.2). By lowering p_v to 0.18, which Lim et al. (2005) used in their STM of Eros, crater fractions of 0.3–0.9 fit the data (Fig. 8), which agrees with the average roughness of 0.3–0.4 that we found for the NIR spectra. This geometric albedo is different from the NEAR derived value that we used in the NIR models, but is consistent with with 10 and 20 μm radiometry (Morrison, 1976).

The STM includes many simplified assumptions and few adjustable parameters beyond the albedo. Effects due to shape, surface roughness, and phase effects from scattering and self-shadowing are all combined in the beaming parameter, which is a scaling factor to the observed flux. Howell et al. (2018) showed how under some circumstances, these effects can act in opposite directions, and in complex ways. Separating these effects is beyond the scope of this paper, and will be further addressed in future work. If we adjust the emissivity, a compensating change in shape or surface topography or adjustment of surface roughness or thermal inertia can give an equivalent model. The apparent contradictory visible albedo values may in fact be due to such additional factors, not accounted for explicitly in the STM. Assuming that the bolometric emissivity has an average value of 0.9 is reasonable for most rocky materials, which are measured to lie within a range of 0.85–1.0 (Maturilli et al., 2016; Ostrowski and Bryson, 2020). Some local materials or locations on Eros might have larger deviations over limited wavelength ranges, but group 1 spectra seem to require crater fraction of 0.4 or less, and the mid-IR requires 0.3 or more. A lower emissivity value would require a lower surface roughness to produce the same model flux. Therefore, a very low average emissivity seems to be ruled out over most of the surface of Eros.

4. Discussion

Although we initially assumed uniform thermal properties and tried to find a set of thermophysical parameters that was consistent with all 25 spectra, as shown in Figs. 4 and 5 no single set of parameters could be found. Instead, our results can be divided into four groups (see Fig. 9) based on the average best-fitting thermal inertia and crater fraction for the members of each group (see Fig. 10).

Fig. 9 shows the sub-solar and sub-observer latitudes for all 18 nights of data we consider here. Because Eros's shape (Gaskell, 2008) and spin state (Veverka et al., 2000) are well constrained by measurements from the NEAR spacecraft, its plane-of-sky orientation can be calculated at the time of each observation with high precision, allowing determination of the particular region of the asteroid's surface from which the spectrum originates. Fig. 10 shows the average thermophysical model results corresponding to the four groups illustrated in Fig. 9.

The orientations of Eros at the mid-times of the spectral observations, divided by group, are shown in Figs. 11–14, along with surface temperature maps for each night's best fitting thermal inertia and crater fraction. We will describe the regions of Eros in the discussion that follows as divided into quadrants, for convenience. Because of its obliquity (Eros's pole is inclined 89° [Vokrouhlický et al., 2005]), Eros has extreme seasons, and is illuminated from one side for several months, and then from the other side for months. This has the advantage

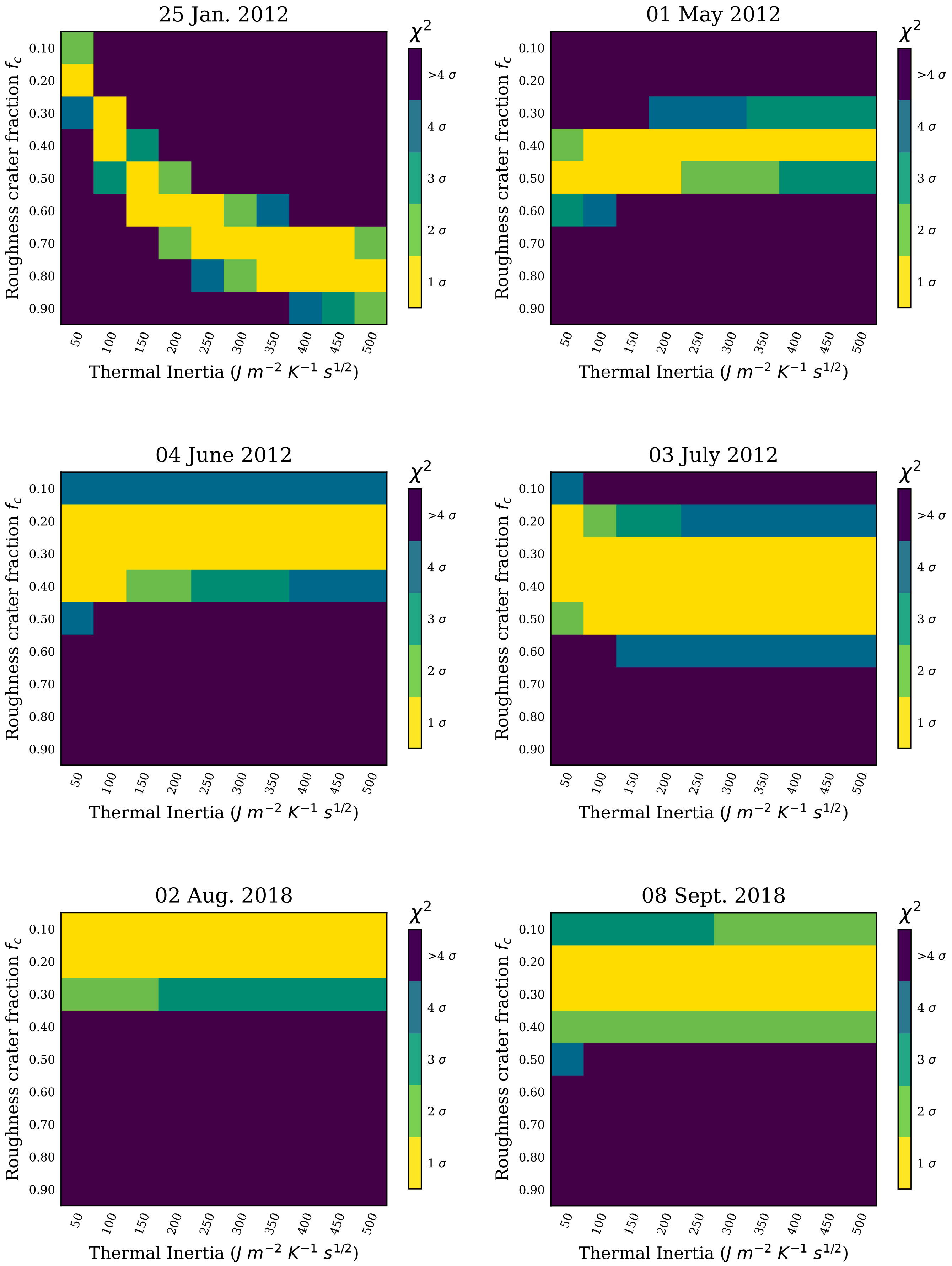

Fig. 4. (*continued*).

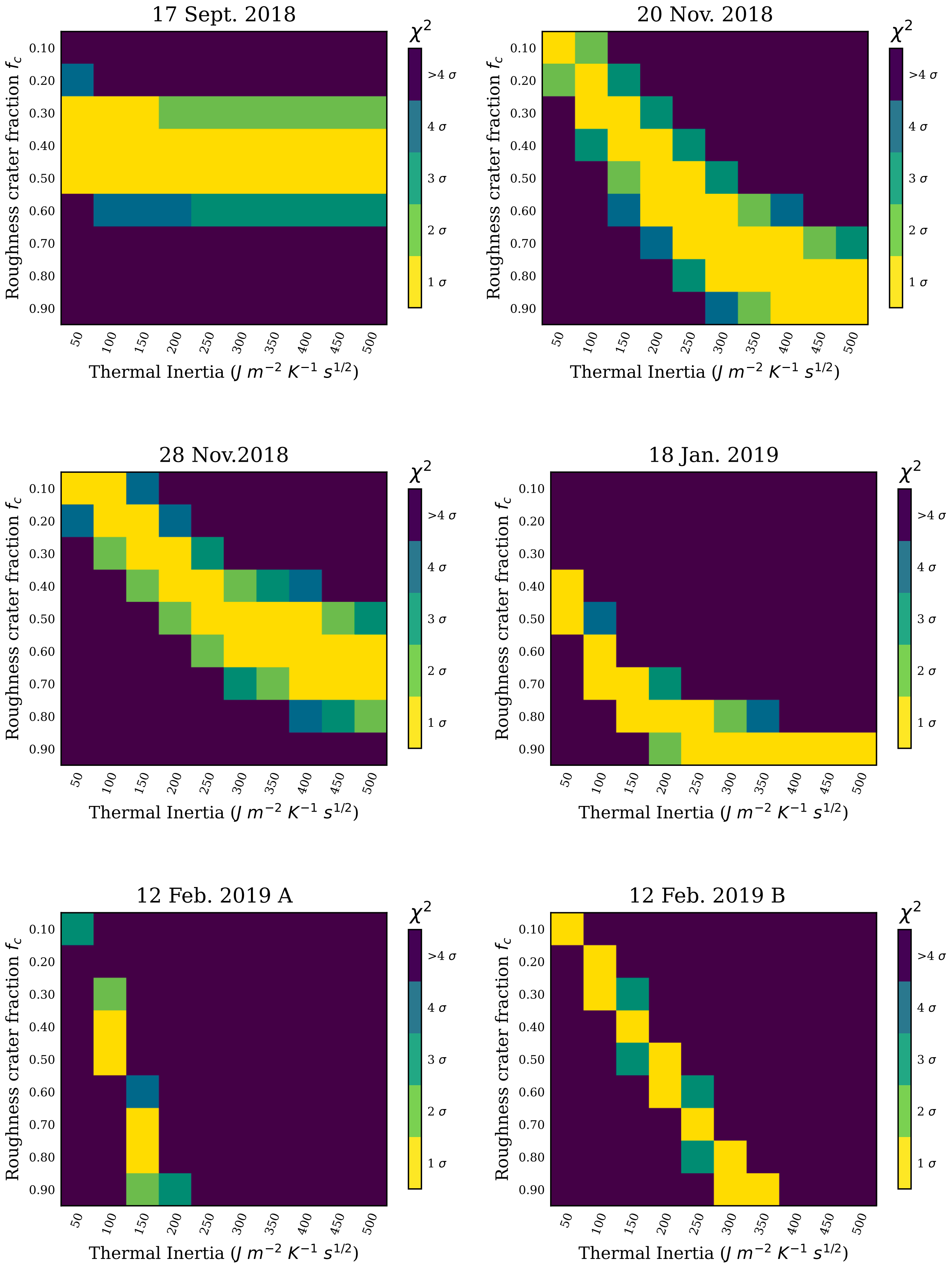

Fig. 4. (*continued*).

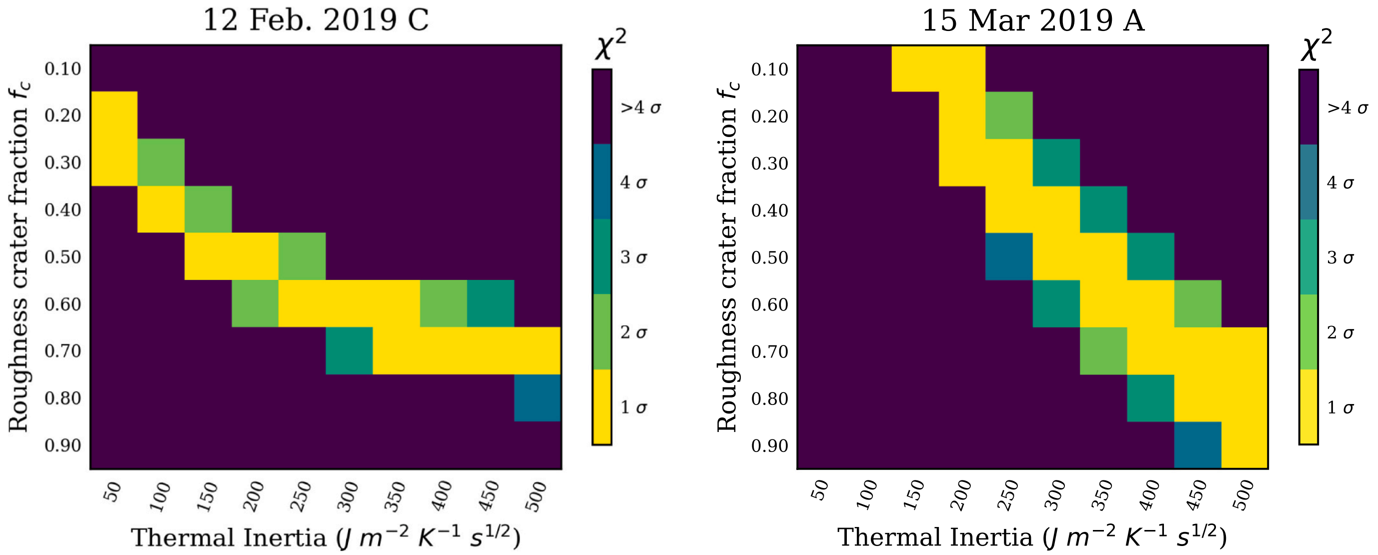

Fig. 4. (*continued*).

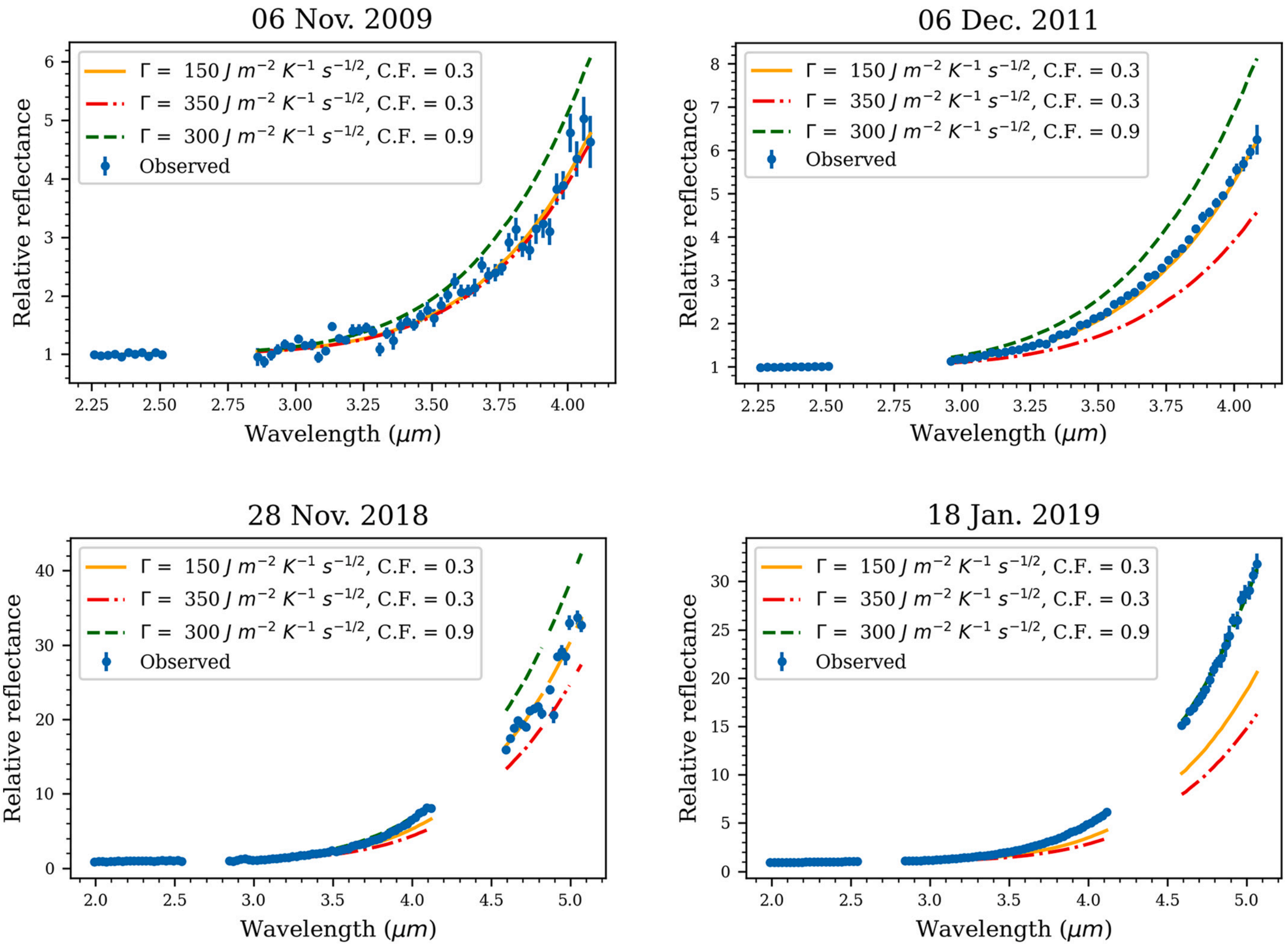

Fig. 5. Comparison of the measured LXD spectrum of Eros for 4 of our 25 observations to thermal models. Each panel shows the particular observed spectrum (blue solid line) along with three representative thermal models (orange solid, green dash, and red dot-dash lines). Each model corresponds to one of the three locales in thermal parameter space that we found were needed to fit all the spectra: Locale A: TI = 100–150 J m^{-2} K^{-1} s$^{-1/2}$ CF = 0.3–0.4, Locale B: TI = 300–400 J m^{-2} K^{-1} s$^{-1/2}$ CF = 0.3–0.4, Locale C: TI = 250–400 J m^{-2} K^{-1} s$^{-1/2}$ CF = 0.9. The remaining LXD spectra are shown in Appendix B. (For interpretation of the references to colour in this figure legend, the reader is referred to the web version of this article.)

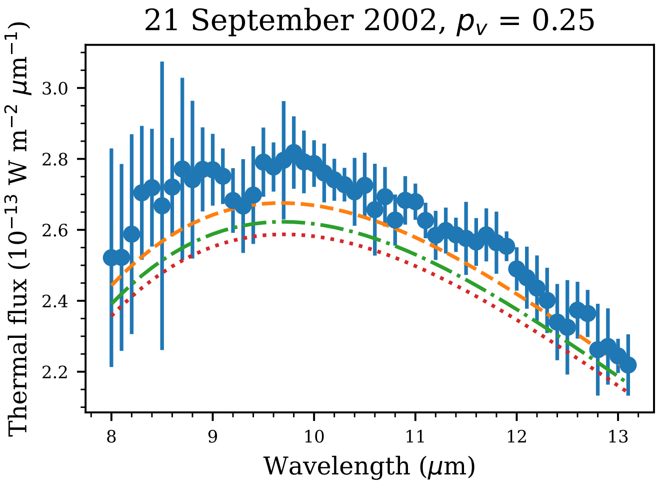

Fig. 6. A mid-IR spectrum from the Palomar Observatory Hale Telescope's SpectroCam-10 is shown with three models. Thermal inertia (Γ, in J m^{-2} K^{-1} $s^{-1/2}$) varies within the average range that we found from NIR thermophysical models in Section 3.2. Thermal inertia does not change the shape of the model spectrum but scales it vertically. Due to the observing and illumination geometry, the scaling effect is extremely small. Using an ISF has the same effect as varying thermal inertia, so we fixed $\Gamma = 150$ J m^{-2} K^{-1} $s^{-1/2}$ and varied the ISF and crater fraction f_c when fitting our mid-IR models.

in that it allows us to separate the thermal properties of these quadrants in observations taken at different times.

Our data cover the near-IR region where the transition from the reflectance regime to the thermal emission regime occurs. Even when the viewing geometry is similar between different observations, we get different thermal measurements when the illumination history has been different, because of Eros's extreme seasons. We cover a range of heliocentric distances, so the absolute scale of our thermal emission varies greatly. However, because we use relative reflectance, only the relative scale changes, so the spectral differences may not appear so dramatic. The thermal modeling, as discussed below, takes this into account and we find that the sensitivity to the thermal parameters can be large at certain orientations, allowing us to distinguish surface areas as well as to constrain the overall average thermal behavior.

4.1. Groups

Turning now to the grouping, the first group (Fig. 10, "Group 1" has a shared set of thermal parameters: crater fraction 0.3–0.4, regardless of thermal inertia value. All observations in this group were made when Eros was more than 1.3 au from the Sun (see Table 1), which resulted in lower equilibrium temperatures. These observations also all had a nearly pole-on illumination and viewing angle. Fig. 9 shows that group 1 populates the upper right and lower left quadrants, where both the subsolar and sub-observer latitudes are high. Any latitude above 30° is effectively "pole-on" on Eros, due to the asteroid's elongated shape and

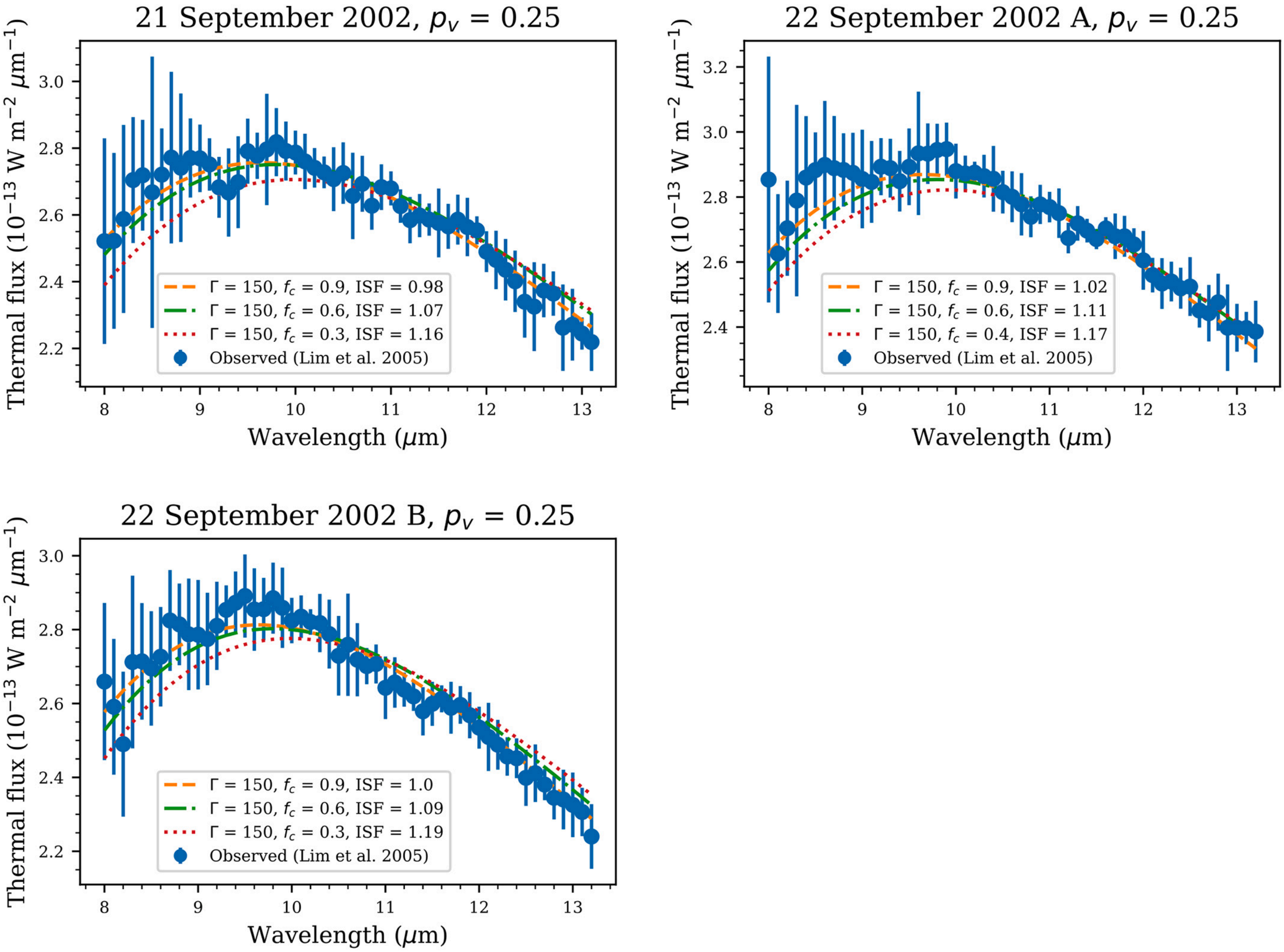

Fig. 7. A range of crater fractions that fit the data at the 1σ level are shown. These models used $p_v = 0.25$, and the $f_c = 0.3$ models do not fit the data at the 1σ level.

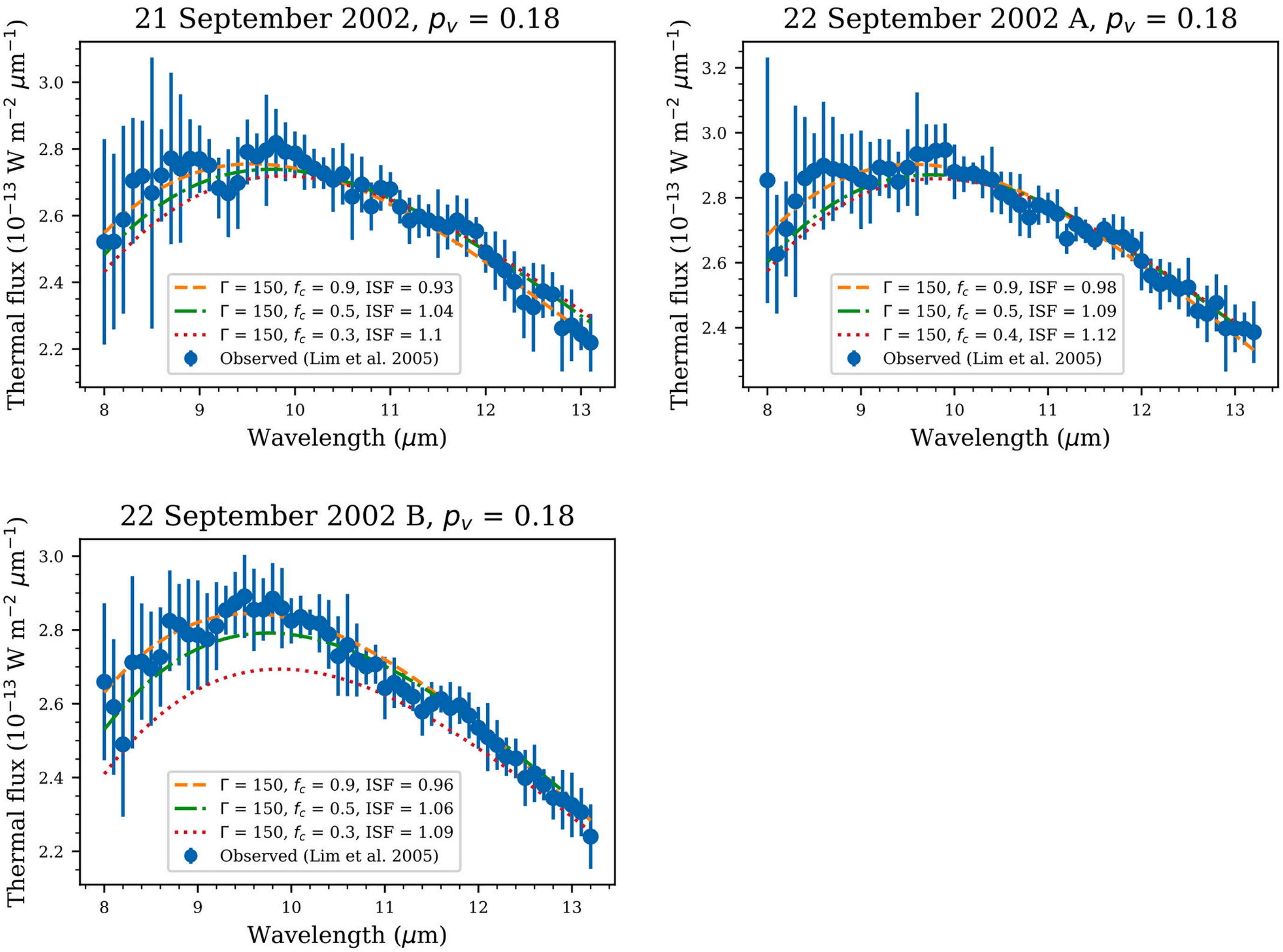

Fig. 8. The range of crater fractions that fit the data at the 1σ level are shown. These models used $p_v = 0.18$, and the $f_c = 0.3$ models fit the data better than the same crater fractions with $p_v = 0.25$.

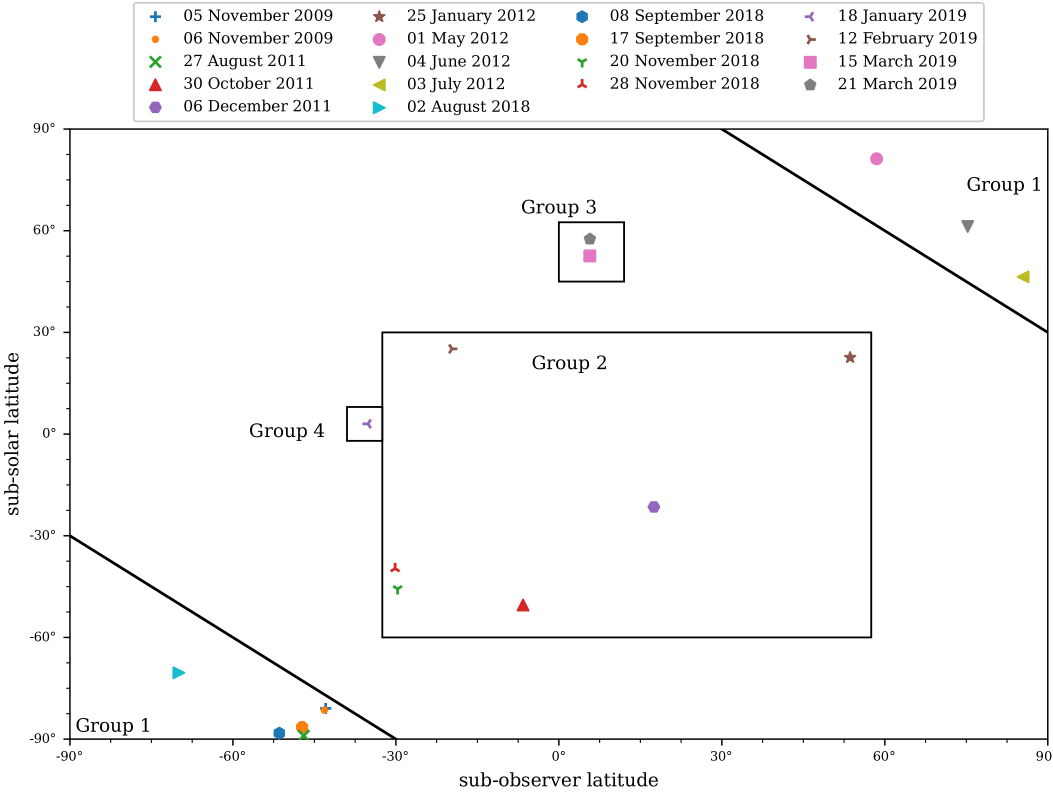

Fig. 9. The latitude of the sub-solar and sub-observer point for each observation of Eros, divided by group. For nights divided into sub-epochs A/B/C (December 2011, Feb-March 2019), the sub-observer and sub-solar point latitudes are taken at the mid-time of the first observation epoch because they do not change significantly between sub-epochs A, B, and C.

obliquity. When Eros's rotation pole is facing the sun, the illuminated hemisphere does not rotate into night for months and the surface is heated continuously. Plane-of-sky images in Fig. 11 show that this endless heating homogenizes the surface temperature distribution, so no individual region or quadrant of Eros dominates the observed spectrum. The lower temperatures and lack of a diurnal thermal cycle combine to make Eros's thermal emission insensitive to thermal inertia, i.e. TI has no effect on the model spectrum's slope here. This means that surface roughness, which is degenerate with thermal inertia, can be constrained by group 1. This roughness result is then applied to the other groups to constrain thermal inertia.

We use the well-constrained crater fraction result from group 1 to constrain two other groups of observations. In the second group, a variety of viewing and illumination geometries are sampled (see Figs. 10 and 13). Unlike group 1, in these observations during the rotation cycle of Eros, the region of surface viewed from Earth changes, showing different regions whose apparent average temperature depends on the thermal inertia. Applying the roughness constraint from group 1 results in a thermal inertia of 100–150, which fits all these observations reasonably well (Fig. 10, "Group 2").

The third group consists of observations made in March 2019 whose best-fitting thermal inertia disagrees with the result from group 2. In these observations, surface roughness of 0.3–0.4 corresponds to a thermal inertia of 300–350 J m^{-2} K^{-1} s$^{-1/2}$ (Fig. 10, "Group 3"). Thermal inertia of 100–150 does not fit these observations well (see the corresponding panels in Fig. 4). The illumination geometry in these observations is effectively pole-on (i.e. sub-solar point is at a latitude >50°; see Figs. 10 and 13), but the sub-observer point is near Eros's equator, again showing the terminator region which changes as Eros rotates and constrains the model thermal inertia.

The fourth and final group solely consists of the observation on 18 January 2019. Fig. 9 shows the unusual viewing and illumination geometry for this particular observation, which is different from that for any of the other three groups of thermal solutions. Only thermal parameters with high surface roughness (0.5–0.9 crater fraction, see Fig. 10, "group 4") fit this observation: the global average thermal inertia is compatible with this spectrum, but the corresponding roughness from groups 1–3 does not fit at the 1σ level. The fact that we can identify this region of extreme roughness is probably due to the viewing and illumination geometry (see Fig. 14), which led us to observe a hot spot on Eros's end. This spot dominates the observed thermal emission, so the inhomogeneous properties of this region on Eros's surface are not washed out by the comparatively cooler surrounding terrain. This suggests localized inhomogeneity that will be investigated in future work.

The average thermal properties of Eros's surface are represented by the 18 observations in groups 1 and 2. Group 1 constrains the surface roughness of group 2, which gives an average thermal inertia of 100–150 and surface roughness of 0.3–0.4. The global average values fit 70% of the observations; they do not fit the remaining 30%. This is related to the interplay among illumination direction, viewing geometry, and Eros's highly elongated shape (see Table 1)). When half of Eros's surface area is illuminated and visible to the observer, the global average thermal parameters fit well. The remaining 7 observations composing groups 3 and 4 do not fit the global average values; they have thermal inertia ranging from 250 to 400 and roughness of 0.3–0.9. This suggests that Eros's thermal properties are inhomogeneous over some small areas; detailed modeling of Eros's surface will be the subject of future work.

Our average thermal inertia result of 100–150 J m^{-2} K^{-1} s$^{-1/2}$ is consistent with Mueller (2007), who used a shape-based TPM to fit a thermal inertia of 100–200 J m^{-2} K^{-1} s$^{-1/2}$, his corresponding roughness adirectional rms slope angle is 44.4° which is higher than our (equivalent) adirectional rms slope angle of 32° ± 4°. Our thermal inertia result is slightly lower than that of Lebofsky and Rieke (1979), who used the

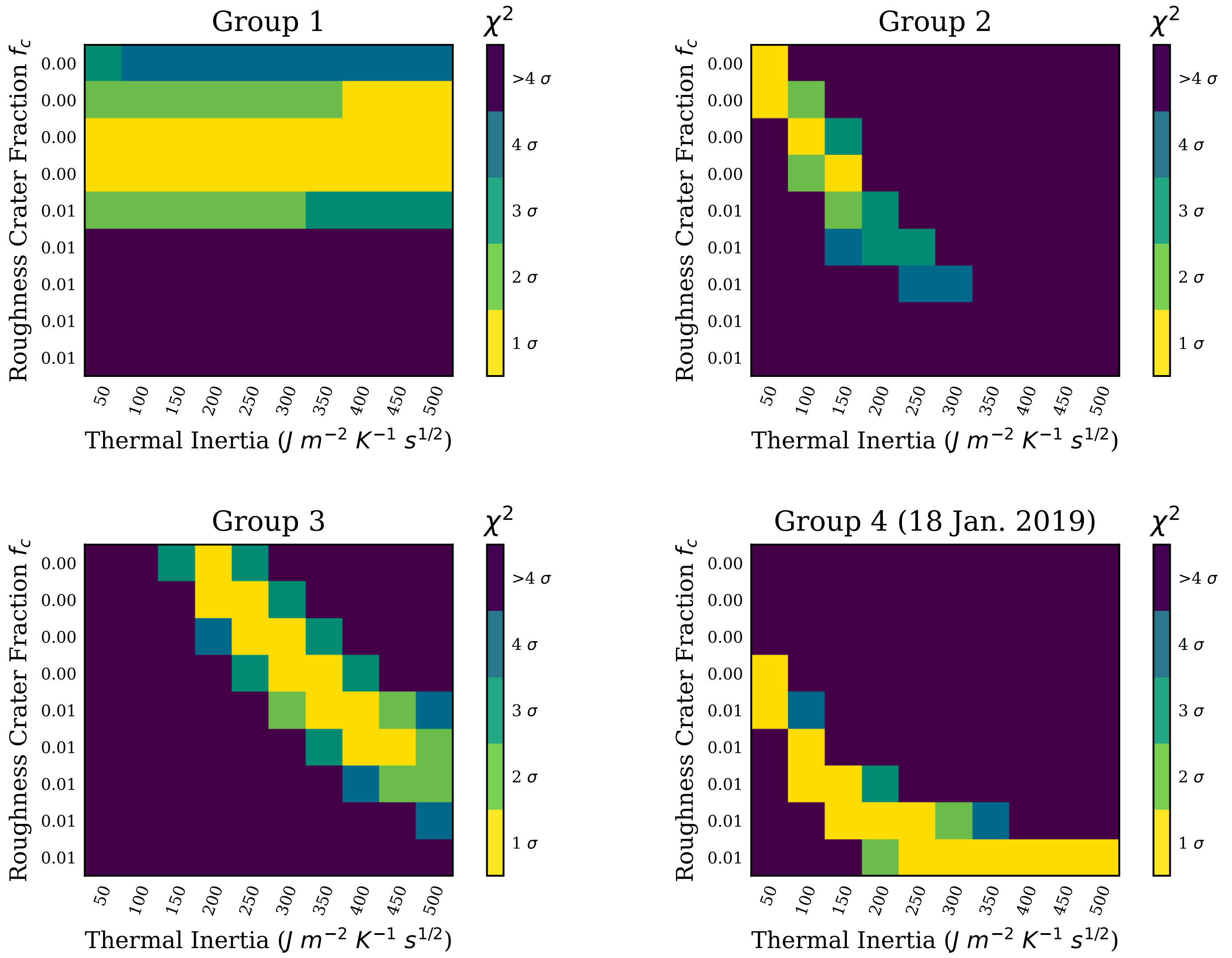

Fig. 10. Best-fitting average thermal inertia and surface roughness for each group. Each yellow square indicates a set of thermal inertia and surface roughness that fit all observations in that group at the 1σ level. Each plot was made by summing the χ^2 maps of the group's members (see Section 3 and Fig. 3). The roughness result from group 1 is used to constrain thermal inertia in groups 2 and 3. (For interpretation of the references to colour in this figure legend, the reader is referred to the web version of this article.)

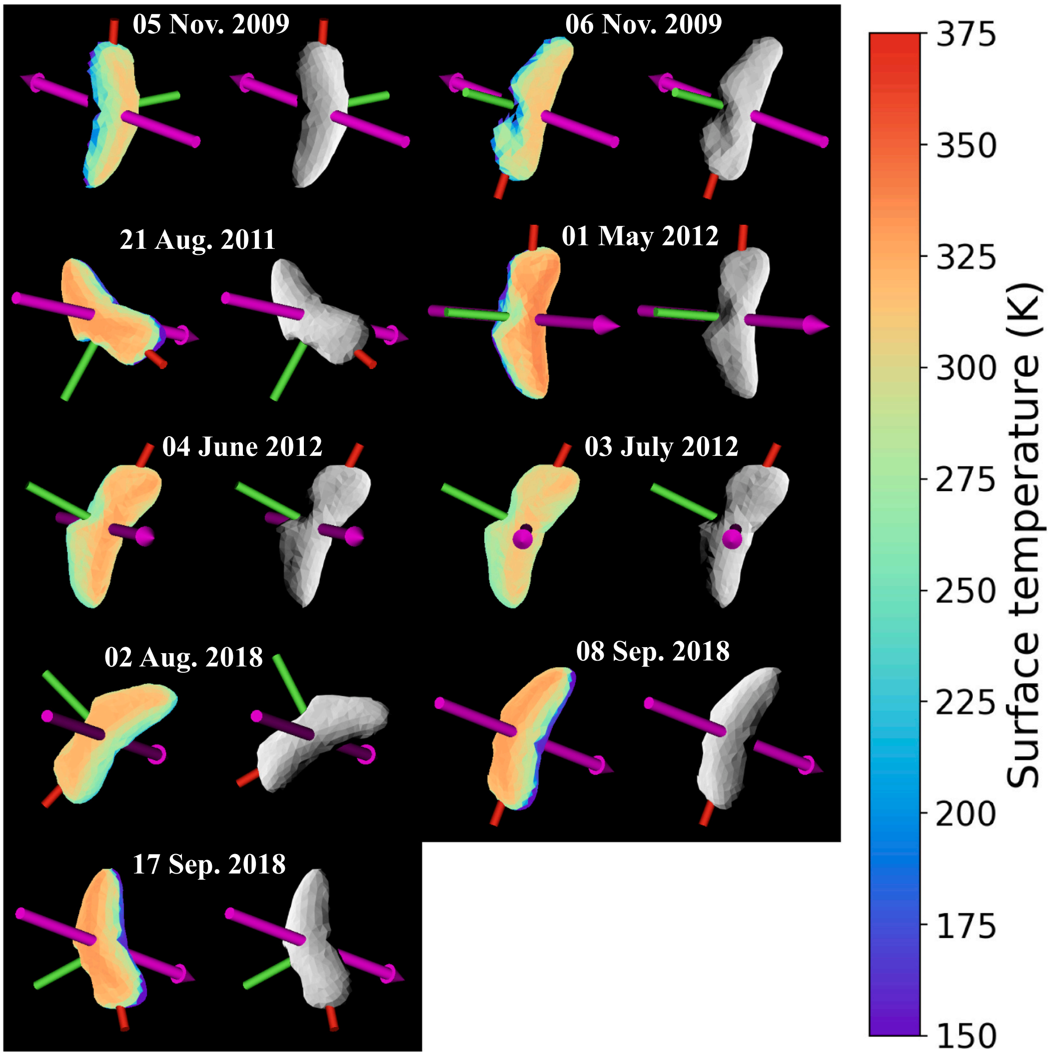

Fig. 11. Plane-of-sky views of Eros at the mid-time of each Group 1 observation from the observer's perspective. Two images are shown for each observation: the rainbow image is a temperature map for each epoch's best fitting combination of thermal inertia and roughness, with red indicating the hottest temperatures and purple the coldest (scale to the right of the figure), the greyscale image shows the Sun's illumination in the optical regime. The magenta arrow is the rotation axis; the other two principal axes are the red and green bars. This group of observations is indeterminate in thermal inertia (see Figs. 5 & 10), but constrains crater fraction to 0.3–0.4. (For interpretation of the references to colour in this figure legend, the reader is referred to the web version of this article.)

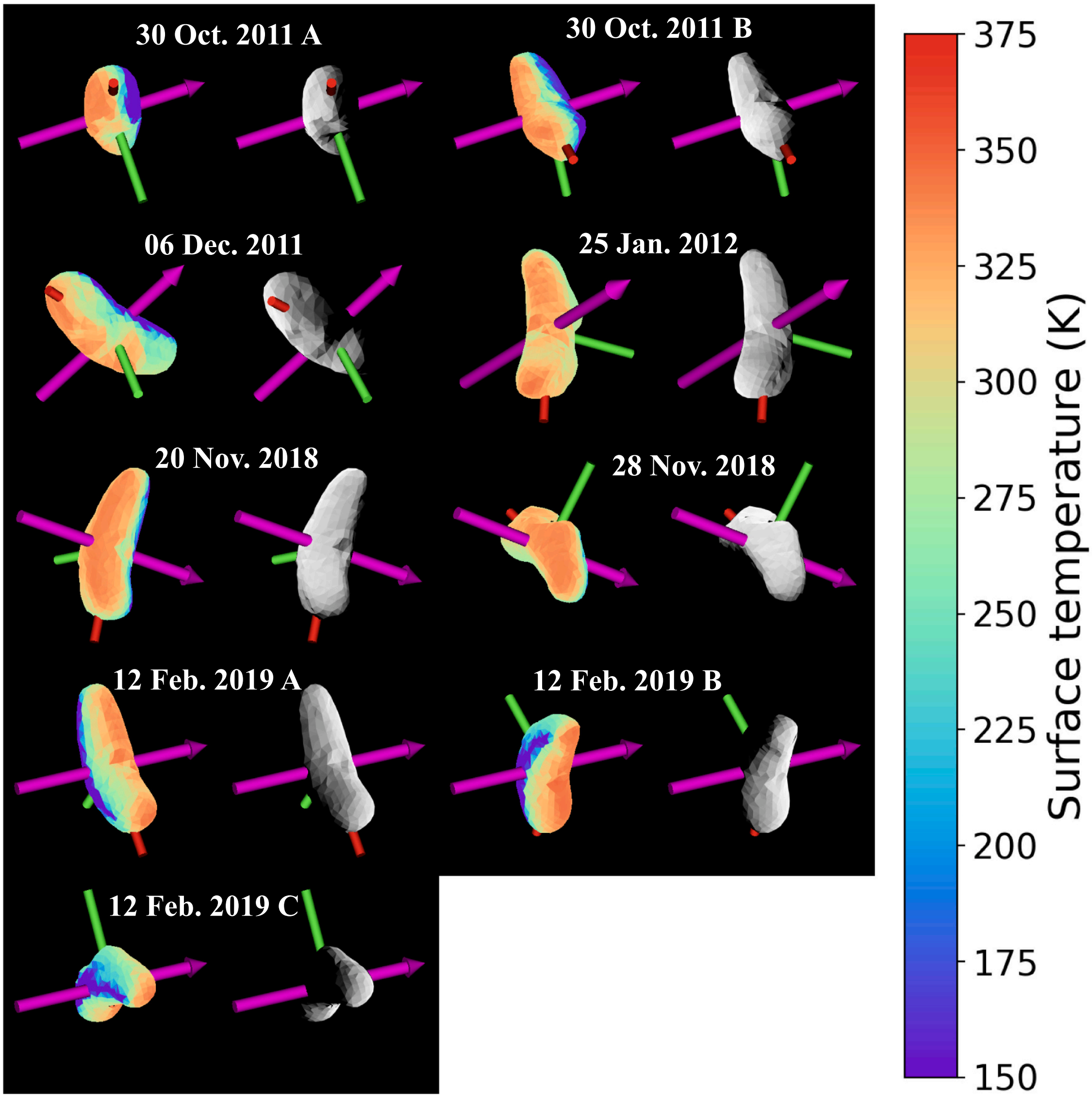

Fig. 12. Same as Fig. 11, but for Group 2 observations. Models with thermal inertia in the range 100–150 J m^{-2} K^{-1} s$^{-1/2}$ and crater fractions of 0.3–0.4 fit all these observations at the 1σ level (See Figs. 5 & 10).

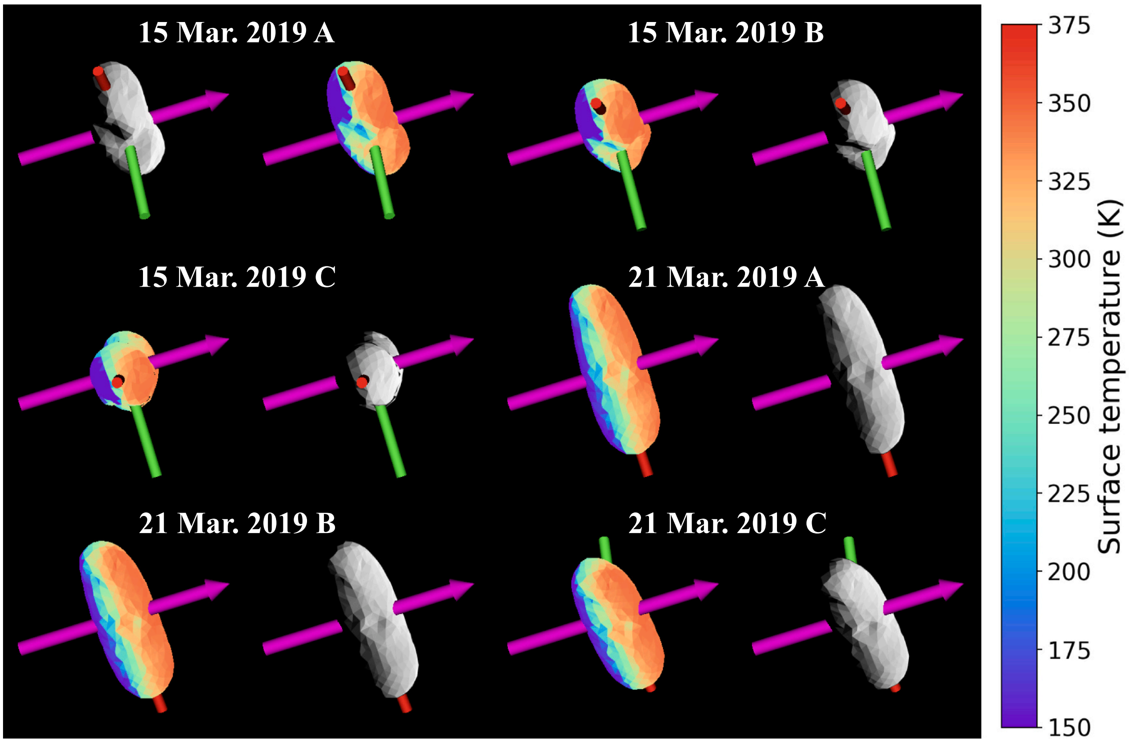

Fig. 13. Same as Fig. 11, but for Group 3 observations. Models with thermal inertia in the range 300–350 J m^{-2} K^{-1} $s^{-1/2}$ and crater fractions of 0.3–0.4 fit all these observations at the 1σ level (See Figs. 5 & 10).

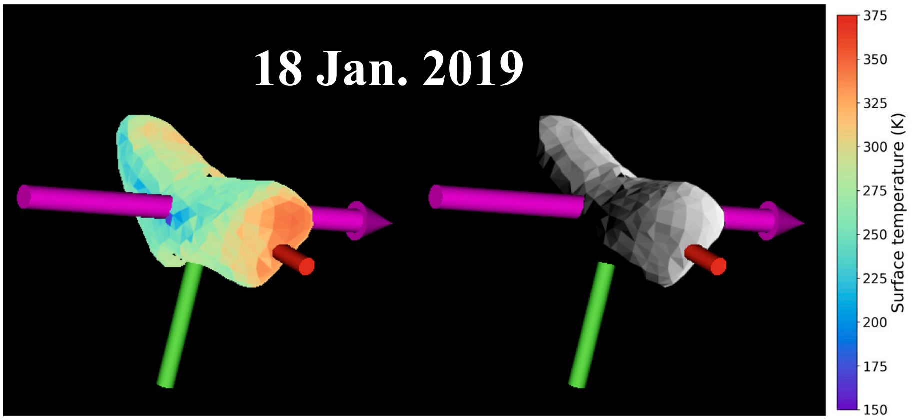

Fig. 14. Same as Fig. 11, but for the single observation in Group 4 (18 January 2019). This observation's best-fitting thermal parameters do not agree with any of the other groups (see Figs. 5 & 10), which may be due to inhomogeneous surface parameters in the hottest region (red spot) dominating the thermal emission spectrum. (For interpretation of the references to colour in this figure legend, the reader is referred to the web version of this article.)

thermal model beaming parameter to estimate a range of 140–280 J m^{-2} K^{-1} $s^{-1/2}$. But their model did not include surface roughness. Our thermal inertia is also lower than that of Harris and Davies (1999) who used the NEATM beaming parameter to estimate thermal inertia of ~170 J m^{-2} K^{-1} $s^{-1/2}$. Rozitis (2017) modeled Eros observations from Lim et al. (2005) to obtain an average global roughness adirectional rms slope angle 38° +/− 5°, which is consistent with our roughness result at the 1σ level. We re-analyzed the Lim et al. (2005) data using SHERMAN and found surface roughness crater fractions of 0.3–0.9 fit well (see Appendix B). This range is very wide and includes our NIR-derived result of 0.3–0.4. Additionally, we found that the geometric albedo assumed for the mid-IR models had to be lower than what we assumed for the near-IR models. This could be due to a wavelength-dependent variation in emissivity, rather than geometric albedo. While wavelength dependent emissivity can be incorporated in our TPM, in the models presented here we use a constant emissivity of 0.9, which is a bolometric value over the range considered (visible to 5 μm). A complete investigation of emissivity effects with wavelength is beyond the scope of this study and will be the subject of future work.

The physical interpretation of thermal inertia and surface roughness remains an open question. Gundlach and Blum (2013) present a method for estimating regolith particle size from thermal inertia measurements, predicting a regolith grain size of 0.2 cm on Eros using T.I. = 150 +/− 25 J m^{-2} K^{-1} $s^{-1/2}$. Most NEAR MSI images have a resolution of 3–19 m (Thomas et al., 2002), too coarse to compare to the predicted grain size. However, NEAR descent images show the surface of a single "pond" region on Eros to be smooth at a scale of 1.2 cm (Robinson et al., 2001), which agrees with a mm-scale regolith grain size. Gundlach and Blum's method was used by Emery et al. (2014) to infer a regolith grain size of 0.17–0.95 cm on (101955) Bennu via thermal inertia obtained from a TPM. This prediction for Bennu is directly contradicted by OSIRIS-Rex's discovery that Bennu's surface is dominated by meter-scale boulders, though high porosity may explain their thermal behavior (Lauretta et al., 2019).

The model hemispherical craters incorporate all sub-scale roughness in a simplified way. If we can link thermal properties derived from modeling of boulder fields, ponds, and other terrain types on the surface of Eros, we may improve our understanding of the physical properties of large blocks on asteroid surfaces and how they contribute to an asteroid's disk-integrated spectrum. Surface roughness may also be different at different size scales. Our global average TPM-derived roughness value is between the value found by Rozitis (2017) via a TPM and his extrapolation of the NEAR Laser Rangefinder's surface roughness to 0.5 cm scale (Cheng et al., 2002; Rozitis, 2017).

Although we were able to find a homogeneous set of thermal parameters that fit 18 out of our 25 observations of Eros equally well in groups 1 and 2, there remains the question of the seven observations in 2019 that do not fit the same range of thermal parameters. These observations probe regions of Eros's surface that the other 18 observations do not. This disagreement suggests inhomogeneity over Eros's surface, particularly between the long and short ends and between hemispheres. In observations where the thermal emission is dominated by flux from a relatively small area of Eros's surface we can isolate the thermal parameters for that local area. January 2019's hot spot, and the opposite hemispherical illumination in October 2011 and March 2019 (see Figs. 12–14), are examples of spectra where the best-fitting sets of thermal parameters do not agree with the homogeneous solution. This suggests that restricted regions of the surface have different properties than the global average. In future work we will identify additional inhomogeneous regions and investigate whether they can be linked to morphological units on Eros's surface identified by NEAR MSI spacecraft images.

5. Conclusion

We present a new analysis of the most comprehensive set of near-IR thermal spectra of Eros ever collected. The data were obtained at a wide variety of sub-Earth and subsolar positions, giving us views of all parts of Eros in various thermal states. By making use of the known shape and spin-state, our data allow us to identify thermal emission from specific regions on Eros's surface, and to assess Eros's global-average thermal properties. Observations of Eros at a variety of viewing and illumination geometries over 18 nights (25 disk-integrated spectra) in 2009–2019 reveal Eros's global average thermal properties. Surface roughness crater fraction of 0.35 ± 0.10 with crater opening angle 130° (equivalent adirectional rms slope angle (ARSA) 32° ± 4°) is constrained by observations made during nine "pole-on" viewing and illumination geometries. Our roughness result agrees at the 1σ level with the ARSA of 38° ± 8° found by Rozitis (2017) and Mueller's (2007) ARSA of 37° ± 8° . Our roughness estimate is most likely lower because of the different parameterizations of roughness used in each model, but when converted to ARSA they agree at the 1σ level.

Our global average roughness crater fraction of 0.35 ± 0.05 is then used to constrain the thermal inertia of two other groups of results. We find that no single value of thermal inertia can fit every observation, regardless of the constraint on surface roughness. Instead, T.I. = 125 ± 50 J m^{-2} K^{-1} $s^{-1/2}$ fits 18 spectra from 2011 to 2019 and agrees with the value of 150 ± 50 J m^{-2} K^{-1} $s^{-1/2}$ found by Mueller (2007). Our global average thermal inertia range for Eros is consistent with Mueller's, and in addition we sample more of Eros's surface. However, the six spectra taken in March 2019 do not agree with our global average thermal inertia result. Those six spectra have T.I. = 350 ± 50 J m^{-2} K^{-1} $s^{-1/2}$. The spectrum from 18 January 2019 requires crater fraction of 0.6–0.8 in order to be compatible with either range for T.I. As shown in Fig. 14, the illumination geometry on 18 January 2019, led to the thermal emission being dominated by a relatively small area of the surface, perhaps with higher than average roughness. These observations show that numerous hemispherical observations can be used to constrain surface regions with thermal properties that vary from the global average. However, the average thermal parameters derived here provide a good representation of most of the surface over most of Eros' orbit.

The relationship between the model roughness, however it is defined, and actual surface morphology is not well determined. Future work will investigate whether thermally inhomogeneous regions on Eros can be linked to morphological units such as craters or regolith ponds identified by NEAR MSI images. If we can demonstrate that spatially resolved asteroid surface properties can be identified from disk-integrated, ground-based observations, this will have important implications for the physical interpretation of thermal inertia and surface roughness on near-Earth asteroids.

Declaration of Competing Interest

None.

Acknowledgements

M. Hinkle acknowledges support from the Center for Lunar and Asteroid Surface Science, a NASA Solar System Exploration Virtual Institute. The authors thank the anonymous reviewers for comments and suggestions which improved the manuscript. All authors but C. Magri were Visiting Astronomers at the Infrared Telescope Facility, which is operated by the University of Hawaii under contract 80HQTR19D0030 with the National Aeronautics and Space Administration. Some of the data utilized in this publication were obtained and made available by the MIT-UH-IRTF Joint Campaign for NEO Reconnaissance. M. L. H. was partially supported by NASA grant 80NSSC21K0658, NASA 80NSSC19K0523 support of Arecibo, and NASA grants NNA14AB05A & 80NSSC19M0214, SSERVI Center for Lunar and Asteroid Surface Science. E.S.H. was partially supported by the NASA OSIRIS-REx Asteroid Sample Return Mission contract NNM10AA11C — Marshall Space Flight Center. S.E.M. was partially supported by NASA Earth and Space Science Fellowship NNX15AR14H. R.J.V., Y.R.F., and C.M. were partially supported by NSF grant AST-0808064. R.J.V., Y.R.F., E.S.H., and C.M. were partially supported by NSF grant AST-1109855. E.S.H. and S.E.M. were partially supported by NASA grant NNX12AF24G. E.S.H., S.E.M., and J. L.C. were partially supported by NASA grant NNX13AQ46G.

Appendix A. Prism and LXD Spectra of (433) Eros

A.1. Prism spectra

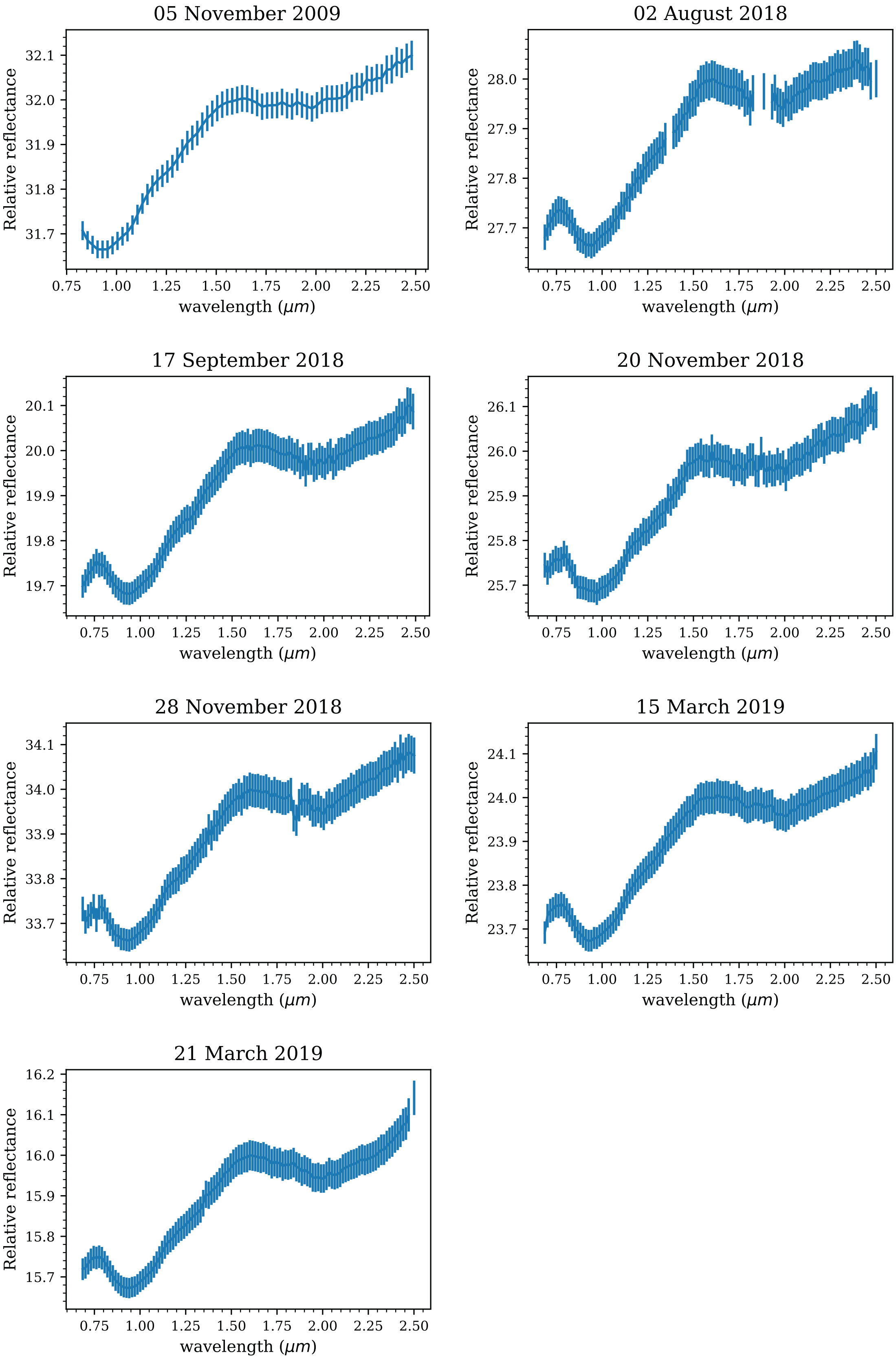

Fig. A1. Eros's reflectance spectrum, observed from NASA IRTF SpeX in prism mode over 7 nights in 2009–2019. The other 4 prism spectra are shown in Fig. 2. Normalization and wavelength ranges are as in Fig. 2. These 7 spectra were averaged with the 4 IRTF prism spectra in Fig. 2 and additional Eros spectra from SMASS and ECAS to produce the average reflectance spectrum in Fig. 3.

A.2. LXD spectra

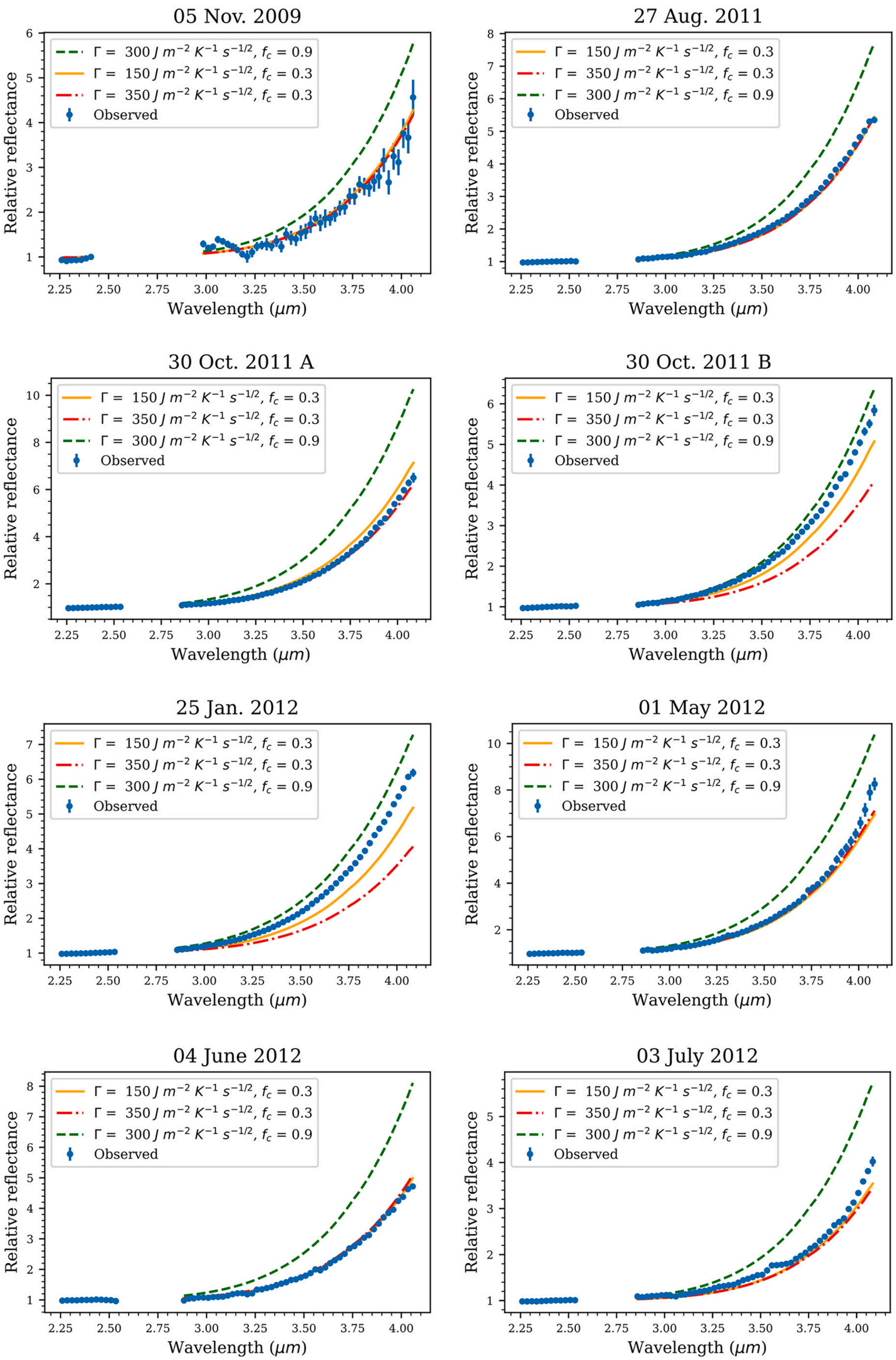
05 Nov. 2009

27 Aug. 2011

30 Oct. 2011 A

30 Oct. 2011 B

25 Jan. 2012

01 May 2012

04 June 2012

03 July 2012

Fig. A2. Comparison of the measured LXD spectrum of Eros for 21 of our 25 observations to thermal models. The other 4 LXD spectra are shown in Fig. 5. Each panel shows the particular observed spectrum (blue solid line) along with three representative thermal models (orange solid, green dash, and red dot-dash lines). The model parameters listed in the legend are as in Fig. 5. (For interpretation of the references to colour in this figure legend, the reader is referred to the web version of this article.)

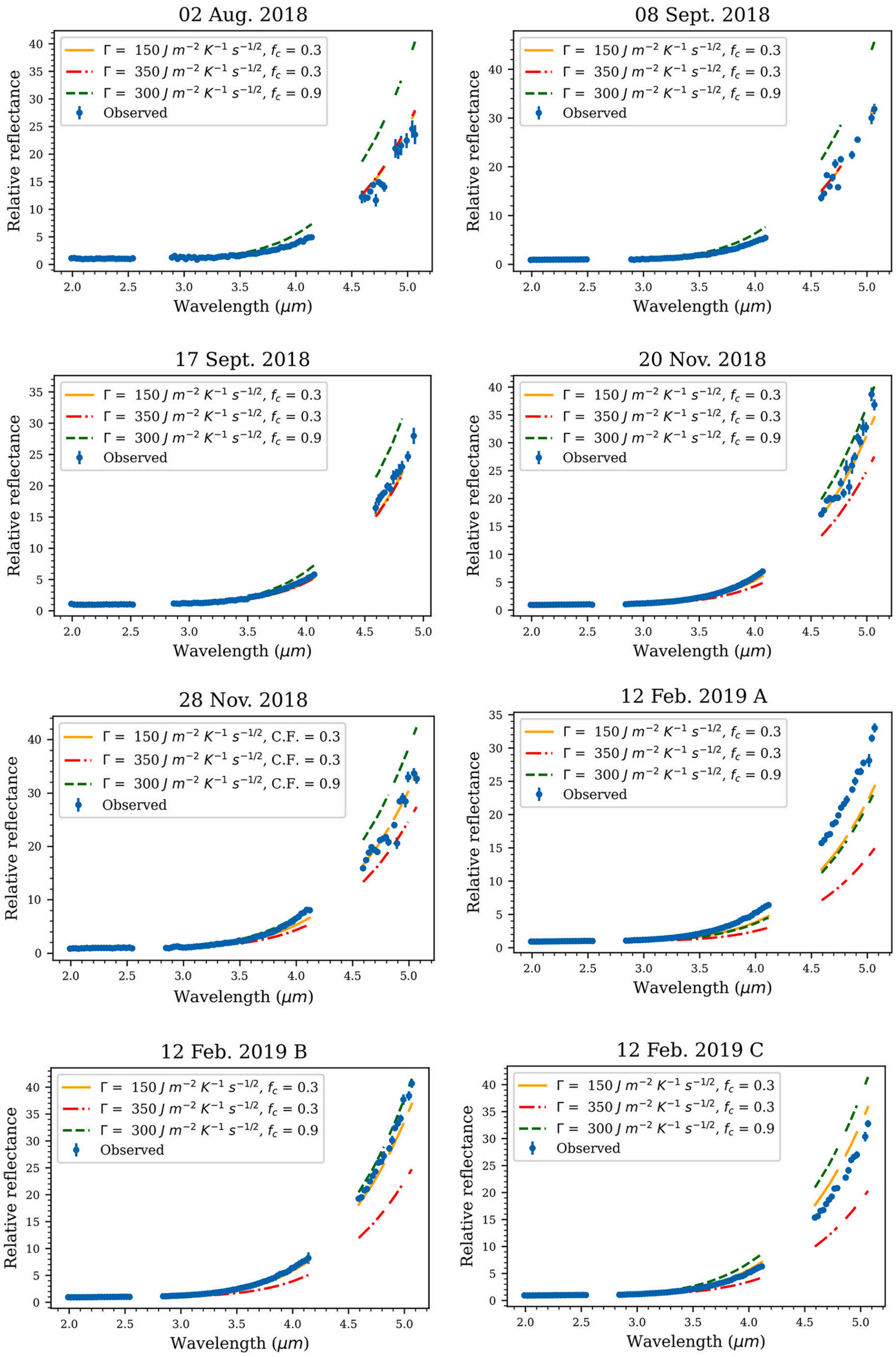

Fig. A2. (*continued*).

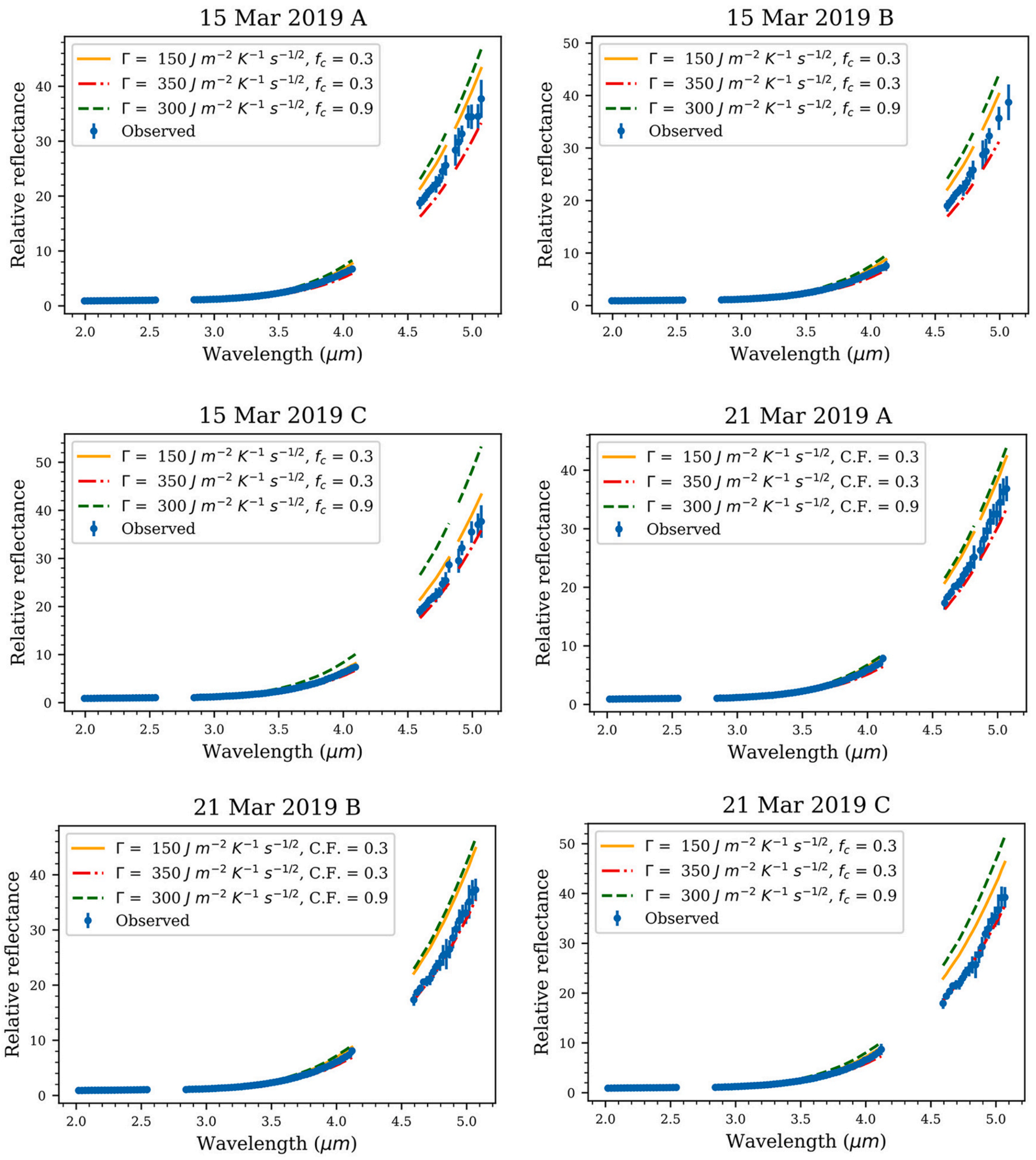

Fig. A2. (*continued*).

Appendix B. Emissivity

The near-IR models presented in this paper assume emissivity ε = 0.9, as is the convention for most other TPMs. Emissivity is not well-characterized for asteroidal surfaces; laboratory analysis of meteorites suggests that silicate meteorites can have ε as low as 0.6 at wavelengths less than 8 μm (Wan et al., 1994; Snyder et al., 1997; Baldridge et al., 2009), while other laboratory analysis of Eros-like ordinary chondrites found that near-IR ε ranges from 0.85–0.9 (Ostrowski and Bryson, 2020). Rozitis et al. (2018) investigated the effect of emissivity in the range 0.5–0.9 for S-type asteroids, finding that lowering ε by 0.1 could lower thermal inertia by as much as 50 SI units.

We tested the effect of different values of ε on some of our models. We found that for the extreme values of ε tested by Rozitis et al. (2018) there was no value of thermal inertia or surface roughness that could compensate and cool the model enough to fit the data. For Group 2 spectra, increasing thermal inertia to high values can cool the surface, and compensate for lower emissivity. However, for Group 1 spectra, changing the thermal inertia has no effect. Decreasing the roughness to zero can compensate for slightly decreased emissivity (ε =0.8). We did find that a modest change to ε of 0.05 could fit the data, but did not push TI or crater fraction outside the global average ranges that we found for Eros. Extreme variation of emissivity over Eros's surface is unlikely, therefore we will continue to assume ε = 0.9 for all our models.

Appendix C. Fine resolution model parameter grid

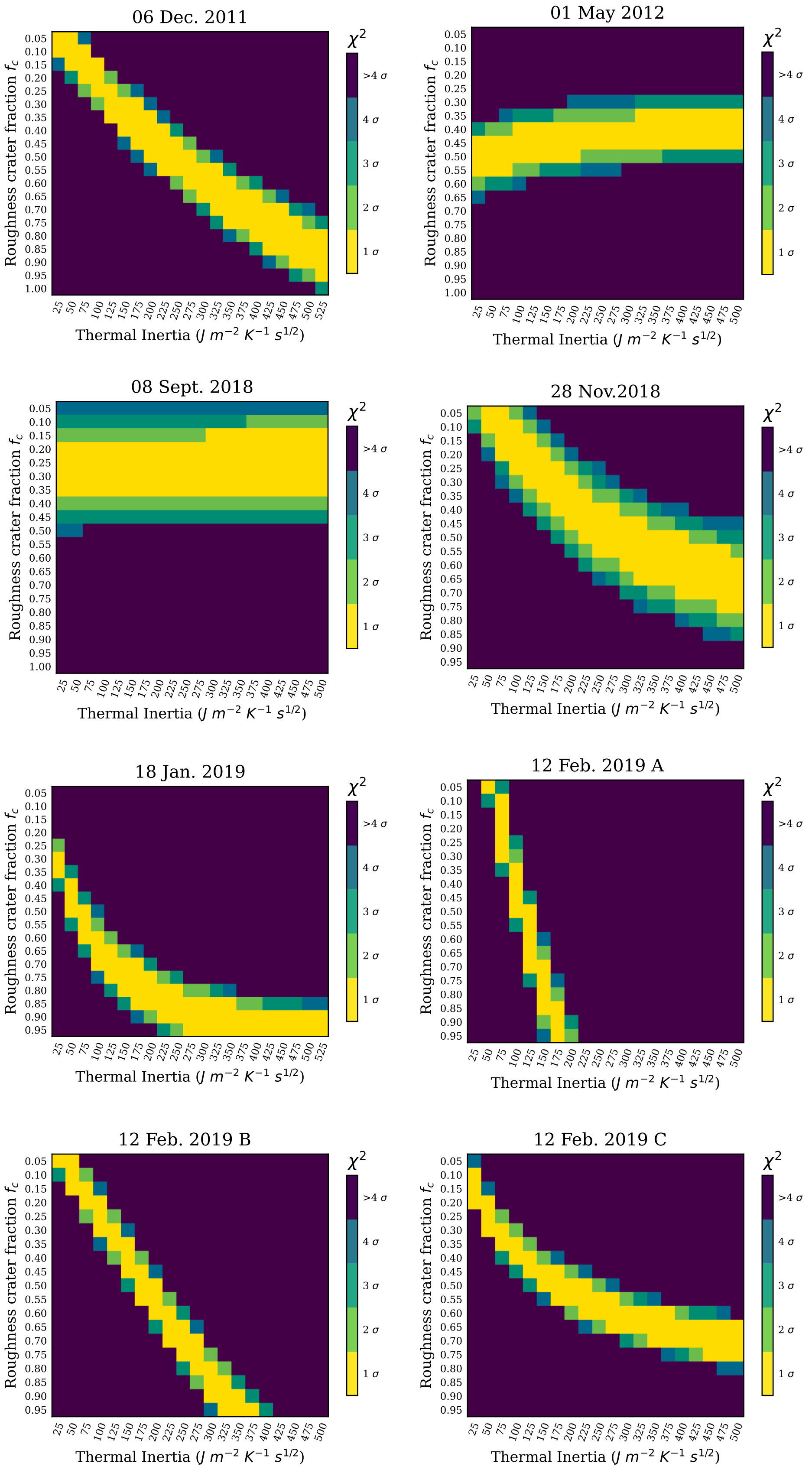

06 Dec. 2011

01 May 2012

08 Sept. 2018

28 Nov.2018

18 Jan. 2019

12 Feb. 2019 A

12 Feb. 2019 B

12 Feb. 2019 C

Fig. C1. The same range of thermal inertia and roughness crater fraction values as in Fig. 5 tested at twice the resolution. The results are the same, so we assume that we can interpolate between squares on the coarse resolution grids.

References

Baldridge, A.M., Hook, S.J., Grove, C.I., Rivera, G., 2009. The ASTER spectral library version 2.0. Remote Sens. Environ. 113 (April), 711–715. https://doi.org/10.1016/j.rse.2008.11.007.

Binzel, Richard P., Rivkin, Andrew S., Scott Stuart, J., Harris, Alan W., Bus, Schelte J., Burbine, Thomas H., 2004. Observed spectral properties of near-earth objects: results for population distribution, source regions, and space weathering processes. Icarus 170 (August), 259–294. https://doi.org/10.1016/j.icarus.2004.04.004.

Cheng, Andrew F., Barnouin-Jha, O., Prockter, L., Zuber, M.T., Neumann, G., Smith, D.E., Garvin, J., Robinson, M., Veverka, J., Thomas, P., 2002. Small-scale topography of 433 Eros from laser altimetry and imaging. Icarus 155 (January), 51–74. https://doi.org/10.1006/icar.2001.6750.

Cushing, Michael C., Vacca, William D., Rayner, John T., 2004. Spextool: a spectral extraction package for SpeX, a 0.8-5.5 micron cross-dispersed spectrograph. Publ. Astron. Soc. Pac. 116 (April), 362–376. https://doi.org/10.1086/382907.

Emery, J.P., Fernández, Y.R., Kelley, M.S.P., K.T. Warden (nèe Crane), C. Hergenrother, D.S. Lauretta, M.J. Drake, H. Campins, and J. Ziffer., 2014. Thermal infrared observations and Thermophysical characterization of OSIRIS-REx target asteroid (101955) Bennu. Icarus 234 (May), 17–35. https://doi.org/10.1016/j.icarus.2014.02.005.

Gaskell, R.W., 2008. Gaskell Eros shape model V1.0. In: NASA Planetary Data System, September, NEAR-A-MSI-5-EROSSHAPE-V1.0.

Gundlach, Bastian, Blum, Jürgen, 2013. A new method to determine the grain size of planetary regolith. Icarus 223 (1), 479–492. https://doi.org/10.1016/j.icarus.2012.11.039.

Harris, Alan W., 1998. A thermal model for near-earth asteroids. Icarus 131 (2), 291–301. https://doi.org/10.1006/icar.1997.5865.

Harris, A.W., Davies, J.K., 1999. Physical characteristics of near-earth asteroids from thermal infrared spectrophotometry. Icarus 142 (2), 464–475. https://doi.org/10.1006/icar.1999.6248.

Howell, E.S., Magri, C., Vervack, R.J., Nolan, M.C., Taylor, P.A., Fernández, Y.R., Hicks, M.D., et al., 2018. SHERMAN - a shape-based thermophysical model II. Application to 8567 (1996 HW1). Icarus 303 (March), 220–233. https://doi.org/10.1016/j.icarus.2017.12.003.

Jones, Jenna, 2018. Investigating Compositional Variations of S-Complex near-Earth Asteroids: (1627) Ivar. PhD Dissertation. University of Central Florida, Electronic Theses and Dissertations. https://stars.library.ucf.edu/etd/5838/.

Lagerros, Johan S.V., 1998. Thermal physics of asteroids. IV. Thermal infrared beaming. Astron. Astrophys. 332, 1123–1132 (1998) 332 (April): 1123.

Lauretta, D.S., DellaGiustina, D.N., Bennett, C.A., Golish, D.R., Becker, K.J., Balram-Knutson, S.S., Barnouin, O.S., et al., 2019. The unexpected surface of asteroid (101955) Bennu. Nature 568 (7750), 55–60. https://doi.org/10.1038/s41586-019-1033-6.

Lebofsky, Larry A., Rieke, George H., 1979. Thermal properties of 433 Eros. Icarus 40 (2), 297–308. https://doi.org/10.1016/0019-1035(79)90074-5.

Lebofsky, Larry A., Sykes, Mark V., Tedesco, Edward F., Veeder, Glenn J., Matson, Dennis L., Brown, Robert H., Gradie, Jonathan C., Feierberg, Michael A., Rudy, Richard J., 1986. A refined 'standard' thermal model for asteroids based on observations of 1 Ceres and 2 Pallas. Icarus 68 (2), 239–251. https://doi.org/10.1016/0019-1035(86)90021-7.

Lewin, Collin D., Howell, Ellen S., Vervack Jr., Ronald J., Fernandez, Yanga R., Magri, Christopher, Marshall, Sean E., Crowell, Jenna L., Hinkle, Mary H., 2020. Near-infrared spectral characterization of solar-type stars in the northern hemisphere. Astron. J. 160 (3), 130 https://doi.org/10.3847/1538-3881/aba0c0.

Lim, L., Mcconnochie, T., Bell III, J., Hayward, T., 2005. Thermal infrared (8-13 Mm) spectra of 29 asteroids: the Cornell mid-infrared asteroid spectroscopy (MIDAS) survey. Icarus 173 (2), 385–408. https://doi.org/10.1016/j.icarus.2004.08.005.

Magri, Christopher, Howell, Ellen S., Vervack, Ronald J., Nolan, Michael C., Fernández, Yanga R., Marshall, Sean E., Crowell, Jenna L., 2018. SHERMAN, a shape-based Thermophysical model. I. Model description and validation. Icarus 303 (March), 203–219. https://doi.org/10.1016/j.icarus.2017.11.025.

Marshall, Sean E., Howell, Ellen S., Magri, Christopher, Vervack, Ronald J., Campbell, Donald B., Fernández, Yanga R., Michael C. Nolan, et al., 2017. Thermal properties and an improved shape model for near-earth asteroid (162421) 2000 ET70. Icarus 292 (August), 22–35. https://doi.org/10.1016/j.icarus.2017.03.028.

Maturilli, Alessandro, Helbert, Jörn, Ferrari, Sabrina, Davidsson, Björn, D'Amore, Mario, 2016. Characterization of asteroid analogues by means of emission and reflectance spectroscopy in the 1- to 100-Mm spectral range. Earth Plan. Space 68 (1), 113. https://doi.org/10.1186/s40623-016-0489-y.

Morrison, David, 1976. The diameter and thermal inertia of 433 Eros. Icarus 28 (1), 125–132. https://doi.org/10.1016/0019-1035(76)90094-4.

Mueller, Michael, 2007. Surface Properties of Asteroids from Mid-Infrared Observations and Thermophysical Modeling. PhD Dissertation. Free University of Berlin. https://refubium.fu-berlin.de/handle/fub188/2368.

Ostrowski, D., Bryson, K., 2020. Laboratory examination of the physical properties of ordinary chondrites. Meteorit. Planet. Sci. 55 (9), 2007–2020. https://doi.org/10.1111/maps.13562.

Rayner, J.T., Toomey, D.W., Onaka, P.M., Denault, A.J., Stahlberger, W.E., Vacca, W.D., Cushing, M.C., Wang, S., 2003. SpeX: a medium-resolution 0.8–5.5 micron spectrograph and imager for the NASA infrared telescope facility. Publ. Astron. Soc. Pac. 115 (March), 362–382. https://doi.org/10.1086/367745.

Rivkin, A.S., Binzel, R.P., Sunshine, J., Bus, S.J., Burbine, T.H., Saxena, A., 2004. Infrared spectroscopic observations of 69230 Hermes (1937 UB): possible Unweathered endmember among ordinary chondrite analogs. Icarus 172 (December), 408–414. https://doi.org/10.1016/j.icarus.2004.07.006.

Rivkin, Andrew S., Howell, Ellen S., Emery, Joshua P., Sunshine, Jessica, 2018. Evidence for OH or H2O on the surface of 433 Eros and 1036 Ganymed. Icarus 304 (April), 74–82. https://doi.org/10.1016/j.icarus.2017.04.006.

Robinson, M.S., Thomas, P.C., Veverka, J., Murchie, S., Carcich, B., 2001. The nature of ponded deposits on Eros. Nature 413 (September), 396–400. https://doi.org/10.1038/35096518.

Rozitis, B., 2017. The surface roughness of (433) Eros as measured by thermal-infrared beaming. Mon. Not. R. Astron. Soc. 464 (1), 915–923. https://doi.org/10.1093/mnras/stw2400.

Rozitis, B., Green, S.F., MacLennan, E., Emery, J.P., 2018. Observing the variation of asteroid thermal inertia with heliocentric distance. Mon. Not. R. Astron. Soc. 477 (2), 1782–1802. https://doi.org/10.1093/mnras/sty640.

Snyder, William C., Wan, Zhengming, Zhang, Yulin, Feng, Yue-Zhang, 1997. Requirements for satellite land surface temperature validation using a silt playa. Remote Sens. Environ. 61 (2), 279–289. https://doi.org/10.1016/S0034-4257(97)00044-8.

Spencer, John R., 1990. A rough-surface Thermophysical model for airless planets. Icarus 83 (1), 27–38. https://doi.org/10.1016/0019-1035(90)90004-S.

Tholen, D.J., 2009. Asteroid absolute magnitudes V12.0. In: NASA Planetary Data System, February, EAR-A-5-DDR-ASTERMAG-V12.0.

Thomas, P.C., Joseph, J., Carcich, B., Veverka, J., Clark, B.E., Bell, J.F., Byrd, A.W., et al., 2002. Eros: shape, topography, and slope processes. Icarus 155 (1), 18–37. https://doi.org/10.1006/icar.2001.6755.

Verbiscer, Anne J., Veverka, Joseph, 1995. Interpretation of the IAU two-parameter magnitude system for asteroids in terms of Hapke photometric theory. Icarus 115 (June), 369–373. https://doi.org/10.1006/icar.1995.1104.

Veverka, J., Bell, J.F., Thomas, P., Harch, A., Murchie, S., Hawkins, S.E., Warren, J.W., et al., 1997. An overview of the NEAR multispectral imager-near-infrared spectrometer investigation. J. Geophys. Res. 102 (October), 23709–23728. https://doi.org/10.1029/97JE01742.

Veverka, J., Robinson, M., Thomas, P., Murchie, S., Bell, J.F., Izenberg, N., Chapman, C., et al., 2000. NEAR at Eros: imaging and spectral results. Science 289 (5487), 2088–2097. https://doi.org/10.1126/science.289.5487.2088.

Vokrouhlický, D., Bottke, W.F., Nesvorný, D., 2005. The spin state of 433 Eros and its possible implications. Icarus 175 (June), 419–434. https://doi.org/10.1016/j.icarus.2004.11.017.

Volquardsen, Eric L., Rivkin, Andrew S., Bus, Schelte J., 2007. Composition of hydrated near-earth object (100085) 1992 UY4. Icarus 187 (April), 464–468. https://doi.org/10.1016/j.icarus.2006.10.034.

Wan, Z., Ng, D., Dozier, J., 1994. Spectral emissivity measurements of land-surface materials and related radiative transfer simulations. Adv. Space Res. 14 (3), 91–94. https://doi.org/10.1016/0273-1177(94)90197-X.

Warren, Jeffery W., Peacock, Keith, Darlington, Edward H., Murchie, Scott L., Oden, Stephen F., Hayes, John R., Bell III, James F., Krein, Stephen J., Mastandrea, Andy, 1997. Near infrared spectrometer for the near earth asteroid rendezvous Mission. Space Sci. Rev. 82 (November), 101–167. https://doi.org/10.1023/A:1005015719887.

Yeomans, D.K., Antreasian, P.G., Barriot, J.-P., Chesley, S.R., Dunham, D.W., Farquhar, R.W., Giorgini, J.D., et al., 2000. Radio science results during the NEAR-shoemaker spacecraft rendezvous with Eros. Science 289 (5487), 2085–2088. https://doi.org/10.1126/science.289.5487.2085.

Zellner, B., Tholen, D.J., Tedesco, E.F., 1985. The eight-color asteroid survey: results for 589 minor planets. Icarus 61 (3), 355–416. https://doi.org/10.1016/0019-1035(85)90133-2.